# LOS-NLOS identification and mitigation based on statistical distributions of LOS and NLOS bias errors

Alex Moschevikin, Sergey Reginya, Alexander Volkov, Alexander Galov, ..., Axel Sikora

***Abstract*—The abstract goes here.**

***Index Terms*—LOS, NLOS.**

## I. Introduction

LOCALIZATION indoors is a challenging problem. Various wireless RF positioning technologies are applied for this purpose: RFID, WiFi, UWB, Bluetooth, ZigBee, nanoLOC, etc. Most of them are based on the measurement of Time-of-Arrival (ToA), Received Signal Strength (RSS), Angle-of-Arrival. In UWB the additional information on the distribution of multipath components is available.

The appropriate positioning accuracy can be easily achieved in Line-of-Sight (LOS) conditions, when the signal propagates at a straight line between a transmitter and a receiver. Unfortunately the larger part of ranging measurements are done in Non-Line-of-Sight (NLOS) conditions. Such measurements contain a certain excess error to the true distance (positive NLOS bias). Thus the main problem is to detect the distance estimations containing NLOS error, and to mitigate the errors during location calculation.

The power envelope of NLOS signals is very complex due to the multipath nature of radio waves propagation. The LOS component is registered first at a receiver, then delayed signals arrive.

The established classification for LOS/NLOS scenarios is the following. If the LOS component is strong, the corresponding channel state is classified as LOS. If it is weak in relation to NLOS components, then channel is considered to be soft-NLOS, or obstructed LOS (oLOS), or NLOS-direct path (NLOS-DP). In case of absence of LOS signal, the conditions are denoted as NLOS, or hard-NLOS.

Although at the moment the majority of investigations in this field are devoted to the UWB radio technology and cellular telephony, the area of this article is nanoLOC sensors networks. The processing of chirp spread spectrum (CSS) signals in nanoLOC is similar to the techniques applied in UWB. Both nanoLOC and UWB are regulated in IEEE 802.15.4a standard.

The research described in this publication was funded by RTL-Service Ltd., Petrozavodsk State University (within the frames of the Strategic Development Program of PetrSU) and supported by the Ministry for Education and Science of Russian Federation and the Ministry for Economical Development of Republic of Karelia (Russian Federation).

Alex Moschevikin is with Petrozavodsk State University and RTL-Service Ltd.

Manuscript received...

The common way to deal with NLOS propagation is to follow three stage process: (1) identification of NLOS conditions, (2) mitigation of NLOS errors, and (3) using the corrected distance data in localization algorithms. In some cases the stages (2) and (3) are combined, in some methods all three stages are iteratively consequently repeated.

There are methods of NLOS identifications based on the analysis of received signal envelope formed by multipath components [1], [2], [3], [4], [5]. Some of these methods operate with the whole set of delayed components, ToA and RSS data, and can be integrated inside the chips at hardware level in order to estimate the distance more accurately.

It is possible to identify the NLOS by using a time series of range measurements [6] especially for moving targets. Some other methods described in [7] also require high repetition rate of ranging. However, the methods based on multiple measurements seem not to be feasible for positioning of many targets simultaneously in a local network indoors: the frequency of measurements is limited by the radio bandwidth and the time duration of one ranging procedure.

In [4] ToA, RSS and RDS (root-mean-squared delay spread) errors estimators are proposed. For the NLOS case the density function for ToA estimates is defined by a convolution of the density functions of measurement noises (Gaussian) and exponentially distributed ToA bias. This ToA estimate has bell-like profile. RSS estimate was modelled by Gaussian with a mean corresponding to the lognormal path loss curve ($\beta_{NLOS}$) and with a certain standard deviation ($\sigma_{NLOS}$).

Montorsi *et al.* [2] proposed an iterative estimator for both the channel state (LOS or NLOS) and the NLOS bias.

NLOS mitigation technique based on residual weighting was developed by Chen [8]. He proposed to suppress those ToA range measurements with larger residuals. However, this method seems to work not perfectly indoors, whereas the majority of measurements contains NLOS error and access points (anchors) are not uniformly distributed.

The technique of mitigation of positive NLOS bias through the analysis of the received waveform was developed by Marano *et al.* [5].

Channel models [9], [10] do not take into consideration any antenna effects (radiation pattern diversity and unknown orientation of antenna). However, in practical commercial installations the performance of all localization engines depends on the accuracy of the path loss (PL) or RSS registration. It is well known that radiation patterns of radio devices are not isotropic. In real conditions the orientation of antenna of

a mobile device is unknown. That results in the substantial uncertainty in RSS due to unknown mutual orientations of two communicating devices. Also the proximity of a human body to a transceiver is unknown beforehand, but it greatly affects the characteristics of radio module. Absorption of radio signals by the human body, antenna mis-tuning, perturbation of a radiation pattern, and change in polarization properties, all these effects are the causes of decreasing radio link budget. For example, the total contribution of these parameters to path loss in 1.9 GHz diapason is estimated between 0.9 dB to 16 dB with average of 3 dB to 10 dB depending on antenna type [11]. The impact of user's hand and head on the total radiated power is also substantial and is analysed in [12]. Obviously RSS estimate in these conditions is unreliable.

As it was said in UWB the researchers work with signals and try to estimate NLOS bias based on maximum signal amplitude, mean excess delay, delay spread, energy, rise time, kurtosis, etc. [1], [2]. NanoLOC hardware does not provide data on the form of the signal's envelope. The chip returns ToA of the first multipath component exceeding a certain threshold value, and the corresponding received signal strength. Realtrac technology [13] developed by RTL-Service Ltd. utilizes round trip time (RTT) scheme for ranging in nanoLOC. Two values of ToA are used to calculate the Time-of-Flight (ToF) and further the distance estimate. Thus ToF and unauthentic RSS estimates are the only input information to identify NLOS conditions.

The intuition is that large distance estimates and small path losses (high received signal power) indicate the conditions of clear LOS. Low path losses evidence no power dissipation due to reflection and/or refraction. At the distances above 100 meters in open space receivers register signals close to the receiver's sensitivity threshold. All multipath components except LOS component are as a rule under this threshold and are not registered.

Low measured distances and relatively high path losses correspond to the NLOS scenario. Reflections decrease the power of a radio wave, so in average the received signal strength is lower for NLOS, than for LOS (interference and diffraction are not considered).

These two simple notions lead to the representation of NLOS bias probability density function as a bell-like profile. If the measured distance in $\hat{d}$, then the true distance $d_0$ is somewhere in the range from 0 to $\hat{d}$ with the certain mean value $d^*$ and the width of the bell $\delta d$.

We propose a NLOS identification technique utilizing this intuitive idea. The goal is to discriminate LOS/NLOS conditions by testing only a single set of ToF and RSS data from a given ranging procedure. The closest approach was described by Alsindi *et al.* [14].

First the statistics for pure LOS conditions outdoors was gathered. Then we carried out a series of experiments indoors and a data base for statistical analysis for NLOS was created. Further analysis revealed the dependencies of $d^*$ and $\delta d$ on the input data (ToF and PL) and made it possible to consider the bias in the positioning algorithms. Thus aim of this study is not only to determine whether the measurement was in LOS or NLOS condition, but to estimate the most probable ToF distance error as well.

The remainder of the paper is organized as follows. Section II contains terms, conditions and expressions concerning the used channel model. Measurement campaign is described in Section III. Section V is devoted to the obtained LOS ToF error profile (LOS TEP) for outdoor conditions. NLOS ToF errors dependencies on ToF and PL data are discussed in Section VI. The proposed model for construction of the combined profile (CombiTEP) for mixed LOS and NLOS conditions is presented in Section VII. Section VIII... Section IX concludes the paper.

!!!TODO!!!

The contribution of this paper is three(?)-fold. A database containing huge number of ToF and PL measurements is presented. The ToF errors pdfs are modelled for LOS and NLOS scenarios. The model of CombiTEP is developed. The work of CombiTEP localization algorithm is demonstrated.

## II. Channel model description

Typical dependence of attenuation of electromagnetic waves in free space on the distance and frequency is described by Friis transmission equation.

$$FSL[dB] = -27,55 + 20 \cdot log_{10}F + 20 \cdot log_{10}d, \quad (1)$$

where $FSL$ denotes Free Space Loss, $F$ is frequency in MHz, $d$ is distance expressed in meters. Obviously, two times increase in distance corresponds to additional 6 dBm in propagation losses in 2.4 GHz radio frequency range.

The path loss is the difference between the output RF power of a transmitter and the measured signal strength at a receiver, i.e. $PL = P_{TX} - P_{RX}$. The distance dependence of the path loss $PL(d)$ in dB is defined as

$$PL(d) = PL(d_0) + 10 \cdot log_{10}(d/d0)^{\beta} + X_{\sigma}, \quad (2)$$

where $d_0$ denotes the reference distance, for example, 1 m, $PL(d_0)$ is the path loss at the reference distance, $\beta$ is the path loss exponent and corresponds to the path loss model, $X_{\sigma}$ describes the RSS uncertainties mentioned in Introduction. $X_{\sigma}$ includes random shadowing effects, unknown antenna gains and cable losses both on transmitter and receiver sides, various mutual orientations of radio modules, human body impact, etc. In the simplest case $X_{\sigma}$ is modelled as a normal distributed variable with zero mean and $\sigma^2$ variance.

Two types of representation of the dependence (2) are shown in Fig. 1. The axis are swapped: in fact the graphs match the dependence $d(PL)$, but not $PL(d)$. In case (a) the vertical axis is expressed in logarithmic scale, in case (b) the values on the axis are linear. The same three $d_i(PL)$ curves with path loss exponents $\beta_1 = 2$, $\beta_2 = 3$ and $\beta_3 = 4$ are plotted on both graphs. For the ease of understanding further in this paper we will use both logarithmic and linear representation of $d(PL)$ according to the context. For the same reason all these curves will be used as reference curves below.

According to [9] the following environments are determined in order to describe the channel model: indoor residential, indoor office, industrial environments, body-area network, outdoor, and agricultural areas/farms. Path loss exponents $\beta$

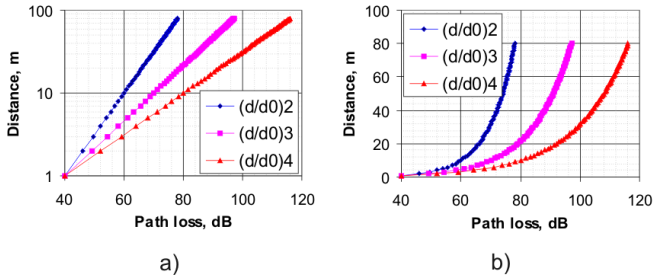


Fig. 1. Distance dependence on path loss $d(PL)$: a) distance axis is in logarithmic presentation, b) distance axis is in linear presentation. The same three $d_i(PL)$ curves with path loss exponents $\beta_1 = 2$, $\beta_2 = 3$ and $\beta_3 = 4$ are plotted on both graphs.

range from 1.6 to 2.0 for LOS scenarios in office environment. NLOS exponents typically range from 3 to 4 for soft NLOS, and 4-7 for hard NLOS [9], [10]. Chehri *et al.* [15] showed that path loss exponent may be as low as $\beta \approx 1.5$ for mines environment since tunnels "focus" the energy through reflections.

Ata *et al.* [16] suggested to consider walls in path loss models. The authors studied attenuation loss factor depending on the number of walls averaged for many building for radiation at 900 MHz and 2.4 GHz. Thus the channel loss model did not correspond to a straight line plotted in Fig. 1a.

The common model for the measured distance $\hat{d}$ is the following [1].

$$\hat{d} = d_0 + b + w, \tag{3}$$

where $d_0$ denotes the Euclidean distance between a transmitter and a receiver (T-R separation), $b$ is NLOS bias, and $w \sim N(0, \sigma^2)$ is the measurement noise.

In UWB the variance $\sigma^2$ of the measurement noise for LOS and NLOS cases is Gaussian and depends on the true distance and the path loss exponent $\beta$ [1], [2].

$$\sigma = \gamma \cdot d_0^{\beta/2}, \tag{4}$$

where $\gamma$ is the proportionality constant. As it will be shown below, it is not true in case of using CSS radio.

### A. LOS/NLOS identification

The idea of the proposed technique of LOS/NLOS identification is the following.

Two curves for LOS and NLOS scenarios with two path loss exponents $\beta_X = X$ and $\beta_Y = Y$ ($\beta_Y > \beta_X$) are plotted on the same picture (see Fig. 2), NLOS curve is to the right. At small distances and low PL values these curves are close to each other, at long distances and high path losses they are far apart. For the same measured distance the LOS signal is stronger than the NLOS signal. It should be mentioned that the vertical axis in Fig. 2 corresponds to the *measured* distance, but not to the true distance as in Fig. 1.

Previous investigations of nanoLOC radio technology revealed no substantial dependence of the *ToF based measured* distance on the PL (for example, see the results in Section V). Therefore in a first approximation the variance of the PL for the certain measured distance can be described by the path

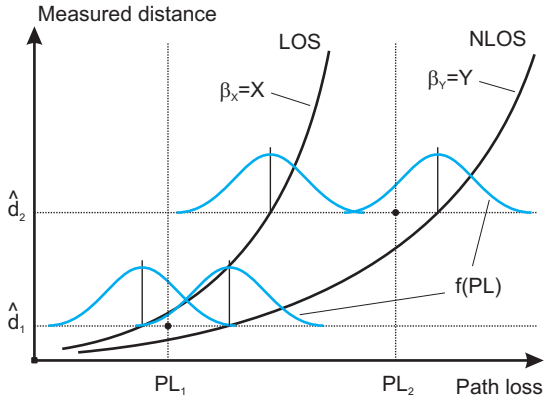


Fig. 2. Measured distance dependence on the path loss

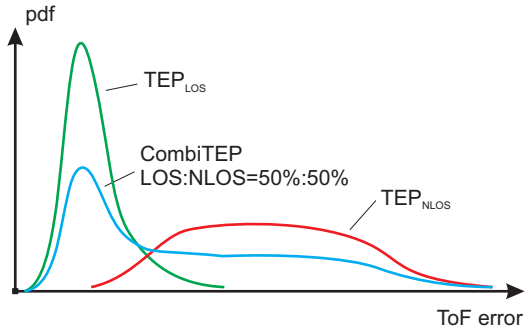


Fig. 3. Construction of the combined ToF error profile from LOS and NLOS errors pdfs

loss pdf ($f(PL)$) with the certain mean and profile width. The examples of $f_i(PL)$ are drawn as blue curves in Fig. 2. Each $f_i(PL)$ corresponds to the certain $\beta_i$ and $\hat{d}_i$ and describes possible various orientation of antennas, human body impact and shadowing effects as well.

Every point on the curve $f_{\beta,\hat{d}}(PL)$ corresponds to the probability of the condition (LOS or NLOS) given the certain path loss exponent $\beta$ and the measured distance $\hat{d}$.

For the point ($PL_2$, $\hat{d}_2$) (see Fig. 2) it is easy to conclude that the path loss $PL_2$ and the measured distance $\hat{d}_2$ correspond to the NLOS conditions. But the point ($PL_1$, $\hat{d}_1$) does not give univocal result. The probability of LOS conditions is higher than of NLOS conditions according to the values of the path loss pdfs $f_{X,\hat{d}_1}(PL)$ and $f_{Y,\hat{d}_1}(PL)$ corresponding to LOS and NLOS.

### B. LOS and NLOS measured distance errors pdfs

Our preliminary results to be published in [17] proved that probability density functions of ToF errors in LOS and NLOS conditions significantly differ. LOS error values are smaller than NLOS bias errors, and LOS probability peak is substantially narrower and closer to the zero (as presented in Fig. 3).

The conditional probabilities of LOS and NLOS scenarios obtained according to the technique described in Section II-A can be utilized in localization algorithms in two ways [14].

The first method is to use only one ToF Error Profile (TEP), i.e. $TEP_{LOS}$ or $TEP_{NLOS}$, corresponding to the largest from the values of $f_{X,\hat{d}_1}(PL)$ or $f_{Y,\hat{d}_1}(PL)$. The second approach is to combine two profiles and to construct the combined ToF error profile (CombiTEP) from LOS and NLOS errors pdfs ($TEP_{LOS}$ or $TEP_{NLOS}$ correspondingly). Fig. 3 illustrates the construction of the CombiTEP whereas both LOS and NLOS components have equal weights.

We will use this second approach. Then CombiTEP might be easily applied both in static localization algorithms and in any type of particle, grid-based, Kalman or other Bayesian motion filter.

## III. Experiments and conditions

The measurement campaign was carried out in Petrozavodsk State University in office environment indoors and in conditions close to ideal outdoors. Inner walls in the building are made from gypsum plasterboard on metal frames.

RealTrac hardware [13] working in 2.4 GHz range and based on nanoLOC transceiver ICs (hand held devices and anchors) was used in all experiments.

In order to speed up the data acquisition we used several hand held device simultaneously. They were put in one box. Orientation of modules inside this box was chaotic.

To obtain the data corresponding to all mutual orientations of antennas in anchors and hand held devices a researcher rotated the packet in front of him. This procedure also introduced human body impact on transmitter's parameters. Rotation of the packet and chaotic orientation of mobile nodes in the box is understood as an averaging procedure for the anisotropic antenna pattern of mobile devices.

The methodology of measurements and general conditions are described in details in [17].

Various experiments indoors and outdoors, as well as registration of antenna radiation pattern of a mobile device were carried out.

The database of all experiments included more than 170,000 entries (see Fig. 4 and Fig. 5). These figures represent the same information. The only difference between them is that the vertical axis in Fig. 4 is logarithmic. Each entry in the database contained the information about the path loss $PL_i$, the straight line distance $d_0$ and the measured distance $\hat{d}$ values.

The registered path loss data are integers converted to dB, whereas the measured distances are floating point numbers. Thus the coloured columns in Fig. 4 corresponds to the discrete path losses.

In Fig. 5 the measurements ($PL_i$ and $\hat{d}_i$) are presented as dots on the plot. In order to show the density of the registered data, some dispersion to the $PL_i$ values was added, therefore path loss values seems to be registered as continuous magnitude. Hereinafter this additional dispersion is applied only for better visualization of results on the plots, the raw data were not affected.

In Fig. 4 and Fig. 5 measurements marked with light blue colour were obtained outdoors in LOS conditions (see the description of the Experiment 2 in Section III-C. Blue colour corresponds to the manually selected data in LOS scenario

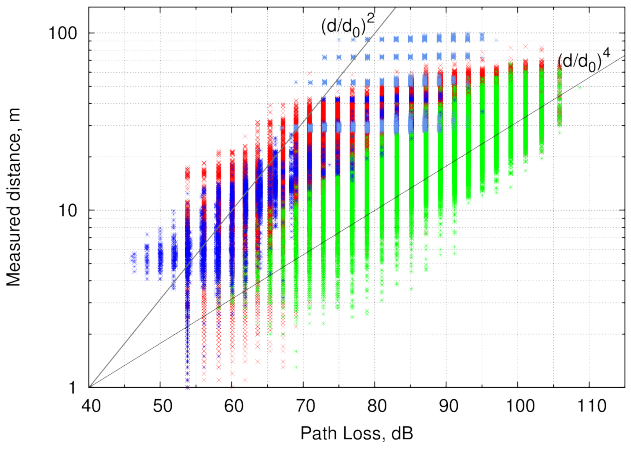


Fig. 4. Raw data summarized for all experiments. The vertical axis is logarithmic. Light blue - data from Experiment 2, LOS, outdoors; blue - data manually selected as LOS scenario, Experiment 3, indoors; red - mixed LOS and NLOS cases, Experiment 3, indoors; green (partly overlay red dots) - NLOS conditions for the communicating devices on the different floors.

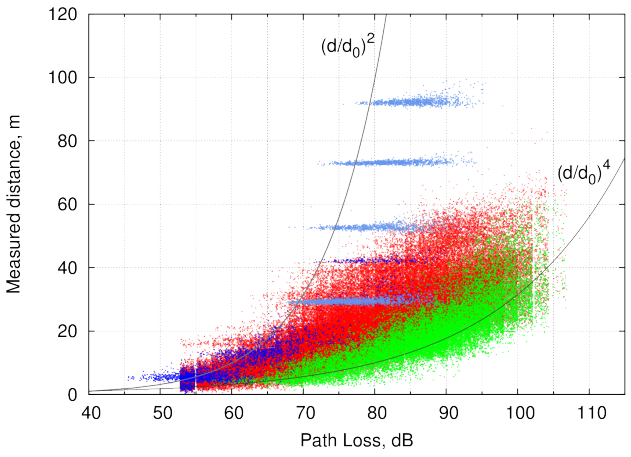


Fig. 5. Raw data summarized for all experiments. The vertical axis is linear. Light blue - data from Experiment 2, LOS, outdoors; blue - data manually selected as LOS scenario, Experiment 3, Series 1, indoors; red - mixed LOS and NLOS cases, Experiment 3, indoors; green (partly overlay red dots) - NLOS conditions for the communicating devices on the different floors. Special dispersion is added to $PL_i$ values for better visualization.

indoors (the Experiment 3, Section III-D, Series 1). Red dots partly belong to the NLOS Experiments 3, Section III-D, series 2 and partly – to the mixed (not identified) LOS and NLOS cases in the Experiment 3, indoors. Green area partly overlays red area. It corresponds to the NLOS conditions for the communicating devices on the different floors (the anchor is on the second floor, the mobile devices are on the third).

The percentage of NLOS measurements in overall volume of the measured data is estimated as more than 85%.

### A. Impact of receiver's non-linearity on path loss registration

In order to correctly process the obtained data it was necessary to consider the non-linearity of path loss registration in some cases. Fig. 6 illustrates this phenomenon.

Output power of a transmitter varies along the horizontal axis. The vertical axis corresponds to the received signal

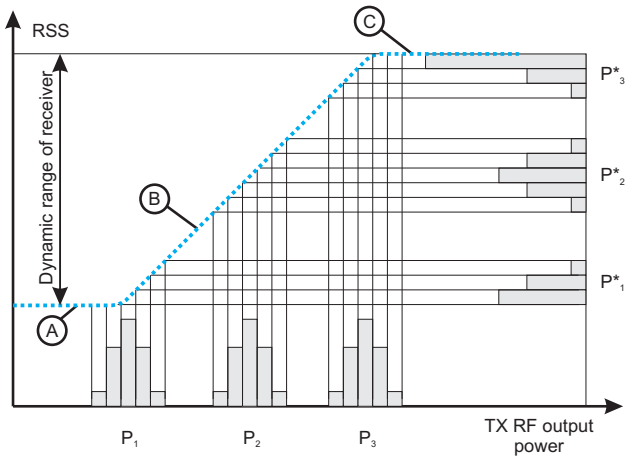


Fig. 6. Non-linearity of receiver characteristics

strength. Channel state conditions vary, the power profile describes these variations. There is a certain distribution in the power of transmitted packets in a series.

As a rule receiver's characteristics are linear in its dynamic range in logarithmic scale (region (B) in Fig. 6). In these conditions input signals are registered without distortion. Power profile $P_2$ of the transmitted and registered signals are the same.

Region (A) is close to the sensitivity threshold of a receiver. All signals below this limit are lost. Thus only a part of the sent packets will be received successfully and power profile will be truncated.

High power signals (region (C)) lead to the saturation of input amplifiers of a receiver. The power profile of the received signals will be distorted. The signals above the threshold will be registered as corresponding to the maximum level.

All the above mentioned non-linearities influence the formation of $f(PL)$ profiles, and therefore should be taken into consideration.

### *B. Experiment 1. Registration of antenna radiation pattern of a mobile device*

As a rule, antenna pattern of embedded and printed antennas in hand held devices is not isotropic. In order to study the antenna patterns of the used hand held devices the following experiment was carried out. A hand held device was mounted on a wooden pole in the middle of the long corridor. It transmitted a frame and the anchor measured the signal strength. The distance between the anchor and the mobile device was approximately 30 meters. Their locations in the building are depicted in Fig. 7.

The mobile node was rotated in three perpendicular planes. In each plane the signal strength was registered for 24 angles corresponding to the $15^o$ step. Thus the antenna parameters were obtained for all orientations in three planes.

Antenna patterns of the used hand held device are presented in Fig. 8. Each plane describes the circular cross section efficiency (sensitivity) of antenna. For example, according to the top-left inset the strength of a signal transmitted by the

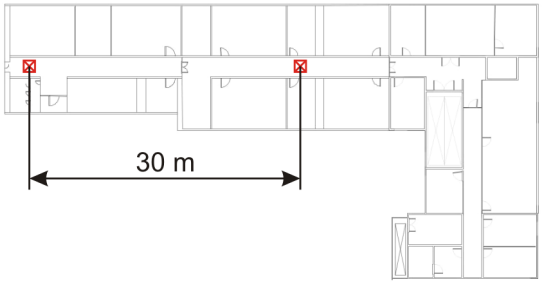


Fig. 7. Scheme of experiment on antenna pattern registration. The anchor (left crossed square) was fixed in the end of corridor. The rotated mobile device (right crossed square) was mounted on a wooden pole.

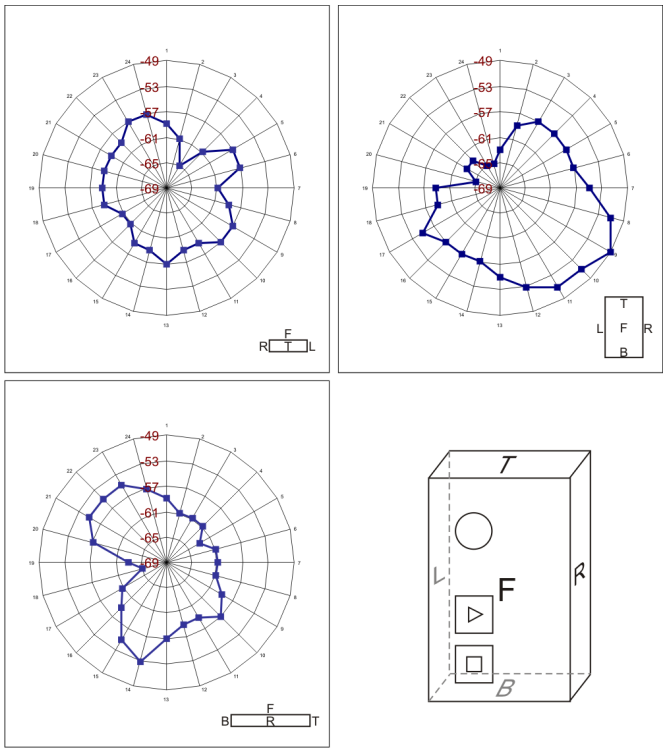


Fig. 8. Antenna radiation patterns of the used hand held device in three perpendicular planes. Letters F, T, R, L and B correspond to front, top, right, left and bottom sides of the device.

mobile device and measured by the anchor in front direction was -59 dBm, and in direction of the left side it was -61 dBm.

Both the anchor and the mobile device had printed pcb antennas. The antenna patterns of other Realtrac devices (access points with embedded antennas, repeaters, tags, radio modules with external antennas) were measured as well, but all them have non-isotropic characteristics.

It should be mentioned that these tests were conducted in a building environment and not in an anechoic camera in order to obtain the "averaged" results *in situ*, not in ideal conditions.

It also should be noted that antennas working in 2.4 GHz range are too sensitive to close surroundings. For example, a device in hand and the same device on a string have different antenna patterns and even different RF efficiency. The path loss value may be 80 dBm in case of matching orientation and polarization between two antennas and 90 dBm or higher

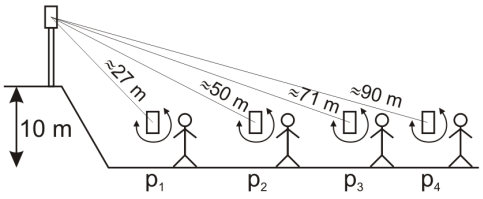


Fig. 9. Scheme of the Experiment 2 outdoors in LOS conditions

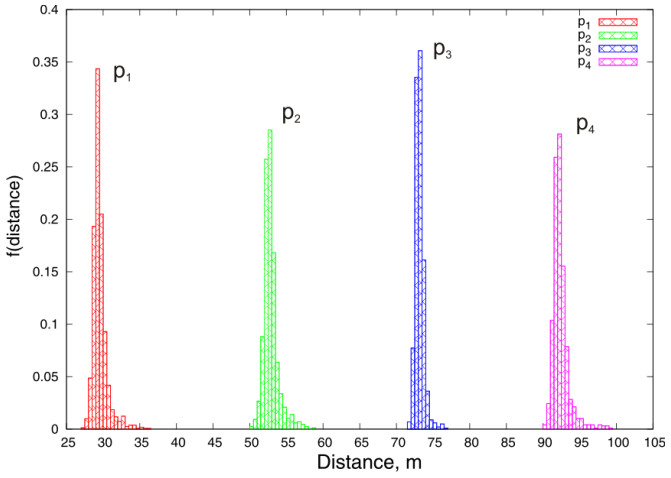


Fig. 10. Estimations of probability density function of measured distances by ToF method of several hand held devices ourdoors in LOS conditions. The horizontal axis corresponds to the *measured* distances.

in case of mismatching.

In real conditions the location calculation software knows nothing about the position of a wireless tag on a human's body, and the tag might be oriented in any direction, and moreover its position and orientation might be changed during the process of tracking the object.

### C. Experiment 2. Outdoors in LOS conditions

The aim of the experiments outdoors was to obtain ToF errors and RSS profiles of chaotically oriented hand held devices in conditions close to ideal open space. Radio signals travel only along the straight line between a transmitter and a receiver without overlapping Fresnel zones.

As depicted in Fig. 9 the anchor module was mounted on a wooden pole on the steep hill. The experimenter rotated a packet with 8 mobile devices in front of him. The RSS and ToF measurements were logged by a computer connected to the anchor. The RSS and ToF profiles were obtained in 4 positions marked as $p_1$, $p_2$, $p_3$, and $p_4$ at different distances: 27, 50, 71 and 90 meters correspondingly. The period of data acquisition was 3 minutes in every position. Mobile devices transmitted radio frames every 1 second.

The histogram of the estimated probability density function of the measured and normalized ToF values is presented in Fig. 10. The size of the bins on this histogram is equal to 0.5 m. The pdf of ToF errors averaged for all positions $p_1$–$p_4$ is characterized by a very narrow peak. The width of TEPs on half-maximum is estimated not to exceed 1.5 m.

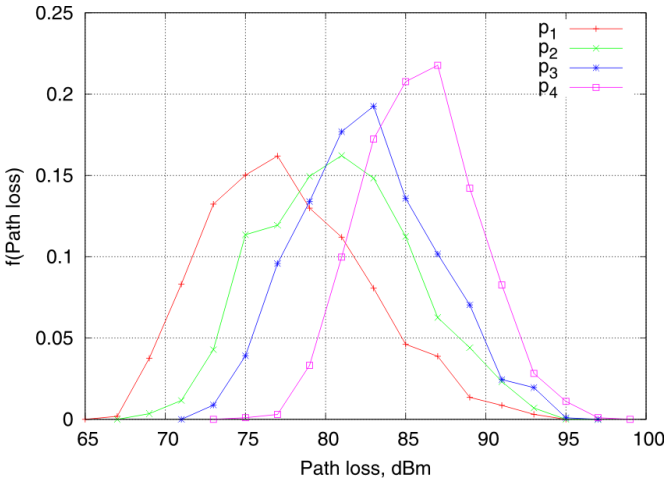


Fig. 11. RSS profiles summarized for several hand held devices ourdoors in LOS conditions in 4 measurement positions $p_1$–$p_4$

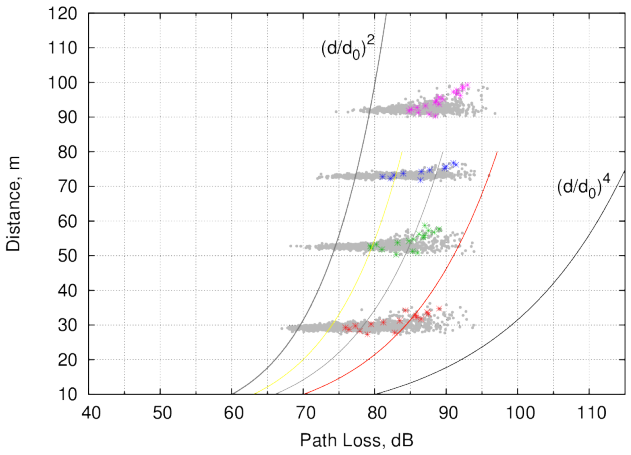


Fig. 12. Raw data for the positions $p_1$–$p_4$ in the Experiment 2. Vertical axis corresponds to the *measured* distance.

The path loss data for the same measurements are shown in Fig. 11. Each RSS and ToF profile includes more than 1400 measurements.

The widths of the RSS profiles on half-maximum for the mobile devices were approximately 12, 12, 10, and 8.5 dBm for the measurements in positions $p_1$–$p_4$ correspondingly.

All the data obtained in Experiment 2 are presented in Fig. 12. Fig. 13 shows the enlarged region of Fig. 12 describing the tests in the position $p_1$.

Red marks in Fig. 13 reveal the correlation between the registered path loss and the measured distance for the constant Euclidean distance. Red marks were set as follows.

First, all values of the measured distances $\hat{d}_i$ in the position $p_1$ were separated into $K$ bins with the bins size of 0.5 m, thus a set of $\hat{d}_k$ ($k = 1..K$) was created. Then for every $k$-th bin the path loss values $PL_{i,k}$ corresponding to the $\hat{d}_{i,k}$ placed in the $k$-th bin were averaged $PL_k = \frac{1}{N}\sum_i^N PL_{i,k}$. The coordinates of the red marks were determined as ($PL_k$, $\hat{d}_k$). The coordinates of green, blue and violet marks in Fig. 12 were calculated in the same way.

The profile formed by the red marks recalls a bell-like func-

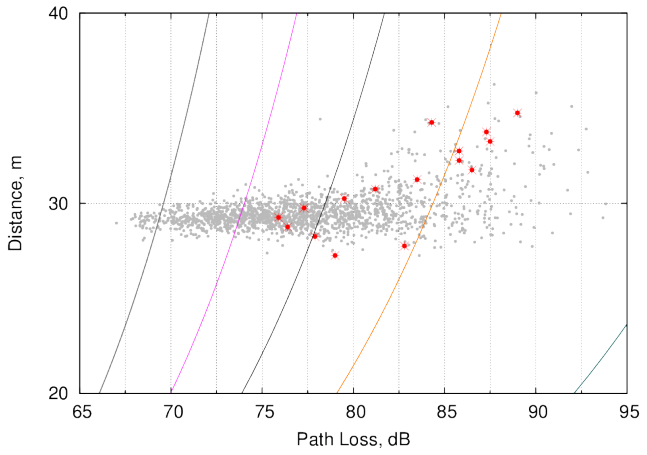


Fig. 13. Raw data for the position $p_1$ in the Experiment 2. Red marks correspond to the centers of the RSS profiles for the certain range of the measured distances with 0.5 m interval. Vertical axis corresponds to the *measured* distance. The true distance was approximately $\approx$ 27 m. Special dispersion is added to path loss values for better visualization.

tion with horizontal axis of symmetry, corresponding to the most probable value of the measured distance (approximately $\approx$ 29 m, see Fig. 13). The wings of this function are not symmetrical. The lower wing (below 29 meters) is shorter, than the wing above 29 meters, since the measured distances $\hat{d}$ can not be smaller that real ones $d_0$.

The ranging accuracy depends on the signal-to-noise (S/N) ratio. The less is the S/N ratio, the worse is the accuracy. The variation in RSS in the experiments was caused by the diversity of antenna radiation patterns of the rotated mobile devices. For low RSS values (high PL values) the uncertainty in distance estimation is much higher than for large RSS values.

For nanoLOC technology almost no dependence of ToF ranging accuracy on the true distance was revealed. Though the profiles in Fig. 12 for the positions $p_1$–$p_4$ formed by the red, green, blue and violet marks correspond to the different true distances (27 m, 50 m, 71 m and 90 m, see Fig. 9), they are similar. Thus the formula (4) is not feasible for CSS based hardware.

However, obviously the variations in the measured distance depends on the received signal strength. In order to analyse the dependence of precision on the RSS we estimate the standard deviation $\sigma_{\hat{d}|RSS}$ of the measured distances for the certain RSS values.

$$\sigma_{\hat{d}|RSS} = \frac{1}{\sqrt{N}} \sqrt{\sum_{i}^{N} (\hat{d}_i - \mu)^2} \qquad (5)$$

Fig. 14 represents the results. The ToF measurements obtained with high power signals has significantly less dispersion, than the measurements carried out with weak signals. It is difficult to derive the law based on these data, but the exponential dependence is supposed.

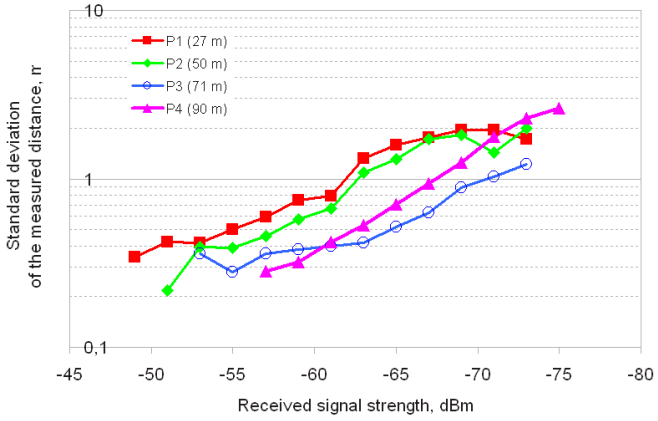


Fig. 14. Dependence of the standard deviation $\sigma_{\hat{d}}$ of the measured distance on the RSS value for the experiments in the positions $p_1$–$p_4$ described in Fig. 12

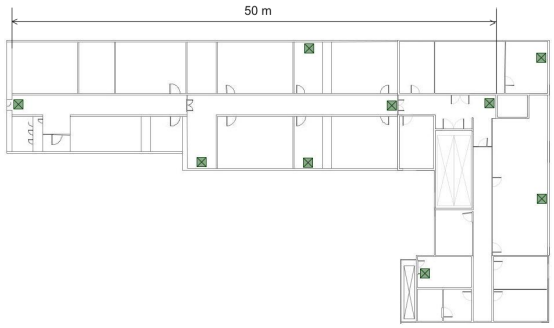


Fig. 15. Positions of anchors on the map of IT-park of PetrSU

### D. Experiment 3. Indoors in LOS and NLOS conditions

Experiments indoors were carried out on the second floor of IT-park of Petrozavodsk State University. The map of the floor is presented in Fig. 15. The length of the central corridor is approximately 50 meters. Nine fixed access point were mounted between the concrete ceiling and light ceiling tiles.

As an example, the coverage area of the *A5B4* anchor is presented in Fig. 16. The mark '*A5B4*' corresponds to the values of the two least significant bytes of MAC-address. The path loss was registered in a hundred of points (tiles). The numbers in 1 meter tiles represent the average path losses in dBm between the *A5B4* anchor and the mobile device rotated by a researcher in a certain tile. Some tiles are gray since signals from those tiles did not reach the *A5B4* anchor. The 20 dBm signal propagates through not more than 5-6 inner walls.

The overall volume of the registered data in the Experiment 3 is presented in Fig. 5 as the red and blue fields of dots.

*1) Series 1. LOS indoors:* The goal of the Series 1 of the Experiment 3 was to obtain LOS data indoors. Some of the registered RSS profiles corresponding to the thirteen positions in the long corridor ($p01$, $p02$, ..., $p13$) between the *A5B4* anchor and hand held devices are presented in Fig. 17. All the data were obtained in conditions of LOS or close to it. In this Series 1 the researcher did not rotated around his axis, but looked in the direction to *A5B4* anchor and

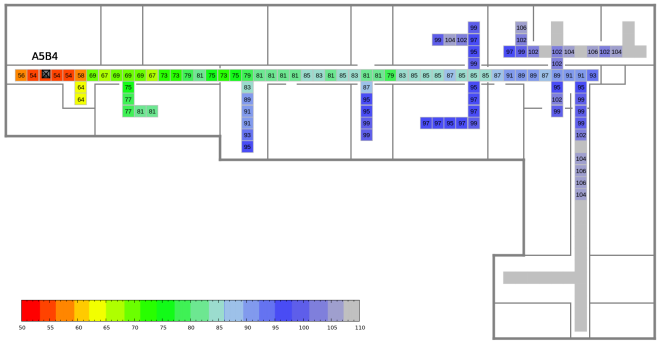


Fig. 16. Typical coverage area of *A5B4* anchor

rotated the packet with mobile devices. In order to obtain the RSS values in all parts of dynamic diapason of receiver, mobile nodes were configured to transmit the radio frames with the known preset power. This output RF power was varied from one experiment to another. Each RSS profile contains approximately 200 processed and normalized measurements.

Table I contains the data on widths of RSS profiles on half-maximum for the curves presented in Fig. 17.

In order to register the low signal power profiles $p01$–$p06$ RF output power of a transmitter was set to -15 dBm. The profile $p09$ corresponds to TX power equal to 0 dBm. Other profiles were obtained for TX power of 20 dBm.

Obviously, profiles $p01$–$p03$ and $p13$ differs from others. $P01$–$p03$ were obtained in conditions close to sensitivity threshold of a receiver, and $p13$ was formed in cut-off mode of the input amplifiers of a receiver (as discussed in Section III-A). These distorted contours were not considered in further calculations. According to the Table I in our experiments the average width on half-maximum of symmetrical RSS profiles ($p04$, $p05$, ..., $p12$) indoors in LOS conditions was approximately 9 dB.

*2) Series 2. LOS and NLOS indoors:* In the Series 2 of the Experiment 3 the RSS profiles in LOS and NLOS conditions indoors were obtained. The data in more than 100 positions was registered. In this series the researcher rotated around his axis and rotated the packet with mobile devices.

Raw data for the Series 2 for mixed LOS and NLOS scenarios are presented in Fig. 18. The vertical axis corresponds to the *measured* distance. The inset histogram describes the probability density function of ToF distance error for all the data on the main graph. The horizontal axis of the histogram is a ToF error expressed in meters, the vertical – the estimation of pdf. Bin size is 0.33 m. The most probable value of ToF error corresponds to $\approx 3.5$ m.

The inset histograms hereinafter are built as follows. For all measurements on the main graph the ToF errors $\varepsilon_i$ were calculated as $\varepsilon_i = \hat{d}_i - d_{0,i}$. Then $\varepsilon_i$ values were distributed on a set of bins. The number of measurements in each bin corresponds to the probability density of the certain ToF error $\varepsilon_i$.

To analyse the pure NLOS scenario, some measurement positions from the whole amount of the experimental data were selected manually. These measurement positions are denoted in Fig. 19 as red dots. The lines connect the positions of the

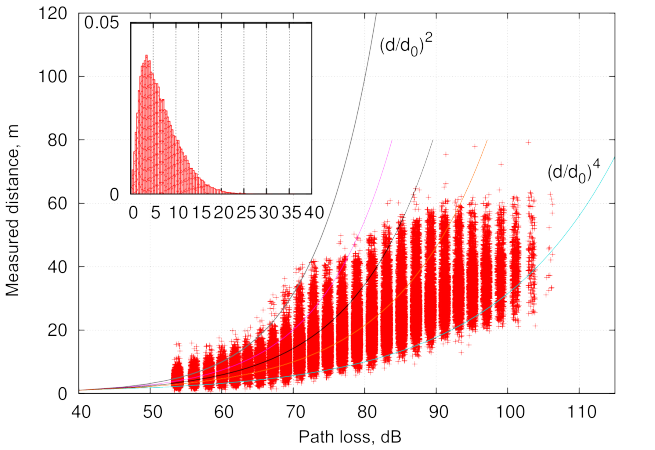


Fig. 18. Raw data for the Experiment 3, Series 2, mixed LOS and NLOS scenarios. The vertical axis corresponds to the *measured* distance. Inset histogram describes the probability density function of ToF distance error for all the data on the main graph (the horizontal axis is a ToF error expressed in meters, the vertical – the estimation of pdf). Bin size is 0.33 m.

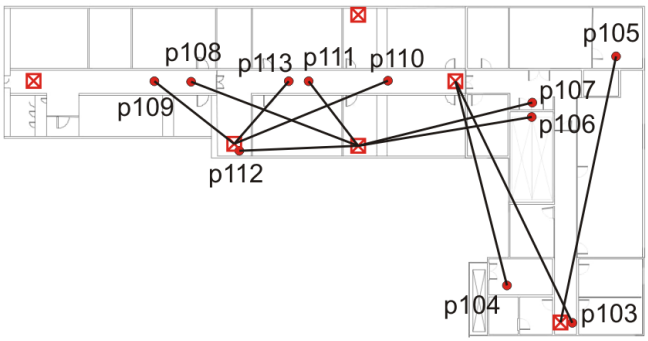


Fig. 19. Measurement positions in Series 2 for NLOS conditions indoors

researcher and the corresponding anchor under the observed NLOS conditions.

The obtained RSS profiles in the positions $p103$–$p113$ are presented in Fig. 17. The profiles consist of 100 measurements in average.

Table II contains the data on widths of RSS profiles on half-maximum for the curves presented in Fig. 17.

The average width on half-maximum of the symmetrical RSS profiles ($p103$, $p104$, ..., $p113$) indoors in the NLOS conditions was approximately 7.4 dB.

*3) Series 3. NLOS different floor indoors:* In order to exclude the LOS case from the ToF errors probability density function the registration of ToF distances and PL was carried out for the mobile devices being on the 3rd floor of the IT-park building whereas the anchors were installed on the 2nd floor. The so called case NLOS-DF (NLOS different floors) was investigated.

Raw data for the NLOS-DP scenario are presented in Fig. 21. The vertical axis corresponds to the *measured* distance. The inset histogram describes the probability density function of ToF distance error for all the data on the main graph. The most probable value of ToF error corresponds to $\approx 6.5$ m.

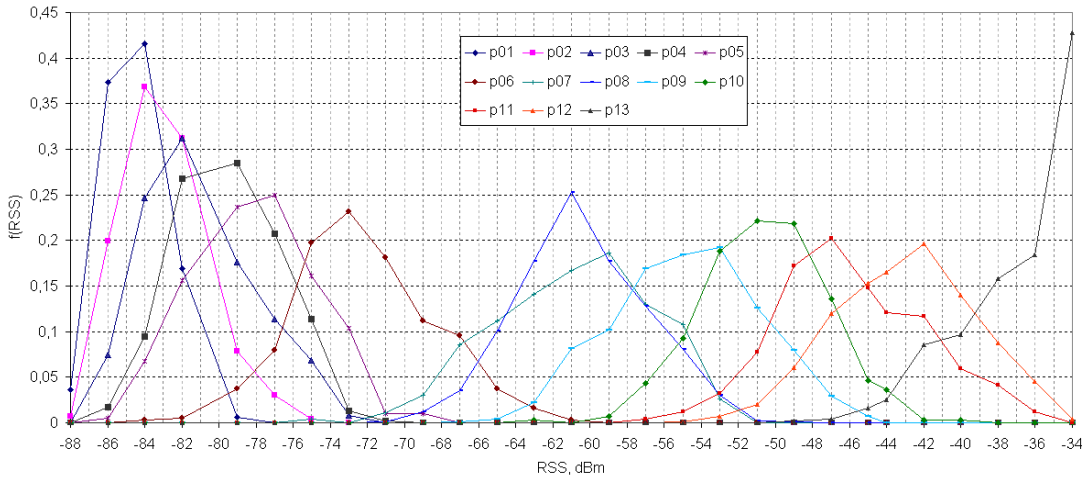


Fig. 17. The normalized RSS profiles for the LOS conditions indoors. The RF output power of a transmitter was set to -15 dBm for the profiles in positions $p01$–$p06$. The profile in position $p09$ corresponds to TX power equal to 0 dBm. Other profiles were obtained for the TX power of 20 dBm.

TABLE I
WIDTHS OF RSS PROFILES ON HALF-MAXIMUM FOR THE CURVES PRESENTED IN FIG. 17 (LOS INDOORS)

| **RSS profile, position** | $p01$ | $p02$ | $p03$ | $p04$ | $p05$ | $p06$ | $p07$ | $p08$ | $p09$ | $p10$ | $p11$ | $p12$ | $p13$ |
|---|---|---|---|---|---|---|---|---|---|---|---|---|---|
| **Width on half-maximum, dB** | 4,5 | 6 | 6,5 | 8 | 9 | 7,5 | 12,5 | 7,5 | 10 | 8 | 9 | 9,5 | 9 |

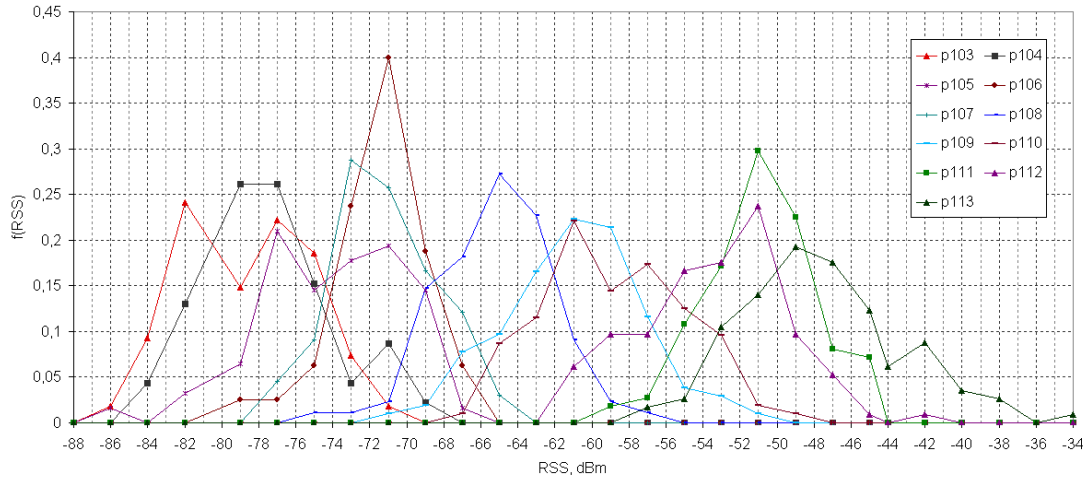


Fig. 20. The normalized RSS profiles for the NLOS conditions indoors. All profiles in positions $p103$–$p113$ we obtained for TX power of 20 dBm.

TABLE II
WIDTHS OF RSS PROFILES ON HALF-MAXIMUM FOR THE CURVES PRESENTED IN FIG. 20 (NLOS INDOORS)

| **RSS profile, position** | $p103$ | $p104$ | $p105$ | $p106$ | $p107$ | $p108$ | $p109$ | $p110$ | $p111$ | $p112$ | $p113$ |
|---|---|---|---|---|---|---|---|---|---|---|---|
| **Width on half-maximum, dB** | 9,5 | 7,5 | 10 | 4,5 | 7 | 8 | 7,5 | 9,5 | 5,5 | 7 | 9 |

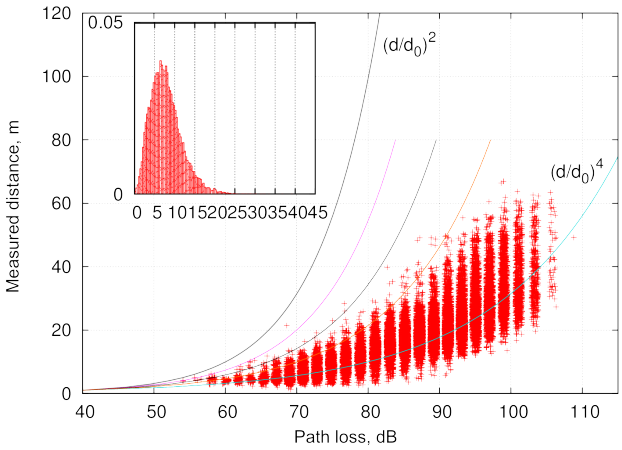


Fig. 21. Raw data for the Experiment 3, Series 3, NLOS-DF scenario. The vertical axis corresponds to the *measured* distance. Inset histogram describes the probability density function of ToF distance error for all the data on the main graph (the horizontal axis is a ToF error expressed in meters, the vertical – the estimation of pdf). Bin size is 0.33 m.

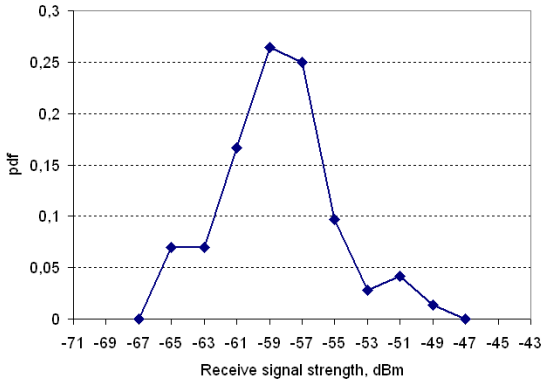


Fig. 22. The modelled RSS profile of the chaotically rotated hand held device

The clear difference between the pdfs in the insets in Fig. 18 and Fig. 21 is that the left wing of the TEP for the mixed LOS and NLOS conditions is much more steeper than for NLOS-DP scenario, and the most probable ToF error value for LOS-NLOS case is less than for NLOS-DP case. Than means that this left wing was formed by the data corresponding to the pure LOS conditions.

Section V is devoted to the derivation of the LOS TEP.

## IV. Unreliability of using the registered path loss in identification of LOS/NLOS conditions

It was mentioned that $f(PL)$ (see Fig. 2 and Section II-A) describes the probability of channel state identification: whether the conditions were LOS or NLOS? In other words it corresponds to the uncertainty of LOS/NLOS discrimination based on the registered PL value. The width of the $f(PL)$ profile correlates with the probability of LOS/NLOS identification error.

The following example illustrates the problem. Let the signal propagates through a wall and it consists only of the LOS component. Intuitively the LOS signal must be strong, but in fact due to attenuation by the wall, the received signal strength is very low. Therefore it is difficult to definitely identify this case as LOS scenario basing only on the PL value: there is large probability to make a mistake. Thus the $f(PL)$ profile should be broad enough not to be zero for the weak RSS (high PL) in LOS conditions in order to consider the LOS "through walls" case in the construction of CombiTEP function.

Otherwise if the line-of-sight is blocked and the conditions for the NLOS component are perfect (polarization and orientation of antenna match, and interference pattern at a receiver module provides local maximum), the received signal strength is strong, that is atypical for the NLOS scenario.

In the analysis below we will try to show that the full width of $f(PL)$ profile for the majority of commercial applications of hand held radio devices is mostly defined by the various mutual orientations of antennas in a transmitter and a receiver, rather than by the measurement noise.

Whereas the ground distance between two radio nodes is constant and the orientation of one of the nodes is unknown, the uncertainty of signal strength can be modelled by the proposed Gauss profile (for example, profiles in Fig. 17 and Fig. 20).

Antenna patterns registered in the Experiment 1 and presented in Fig. 7 are not uniform. The largest received signal strength was $-49$ dBm, and the smallest was $-65$ dBm. The difference between the largest and the smallest values reached 16 dBm.

Evidently three cross sections of antenna pattern presented in Fig. 7 do not completely describe 3D distribution of energy emitted by the antenna. In spite of this in order to obtain the RSS profile of a chaotically rotated hand held device (alike profiles presented in Fig. 11, Fig. 17 and Fig. 20) the following technique was applied. For a device with unknown orientation, its RSS profile of rotating device is formed by all possible orientations. Therefore a histogram was constructed on the basis of the antenna patterns. Values of sensitivities in dBm for all angles in all three cross sections were summarized. The result is presented in Fig. 22.

The width on half-maximum for the modelled RSS profile is approximately 7 dB.

This modelled RSS profile in the first approximation may be described by a Gaussian-like bell curve. In this case RSS value follows log-normal distribution, which is a probability distribution of a random variable whose logarithm is normally distributed. Common equation looks like:

$$G(x) = A_0 \cdot \exp(-\frac{x^2}{2\sigma^2}), \tag{6}$$

where $x$ corresponds to the RSS value expressed in dB, and $\sigma$ – standard deviation. It controls the width of the bell.

The value of full width on half-maximum (FWHM) interval corresponds to $\Delta_{FWHM} = 2.35 \cdot \sigma$. The probability of lying $x$ between the limits $-\sigma$ and $+\sigma$ is 68%, the probability of hitting FWHM interval is approximately 78% (more than three quarters of all data forming Gaussian curve are inside the FWHM).

The center of the modelled contour presented in Fig. 22 corresponds to $RSS_{c,model} = -58.5$ dBm. In order to align

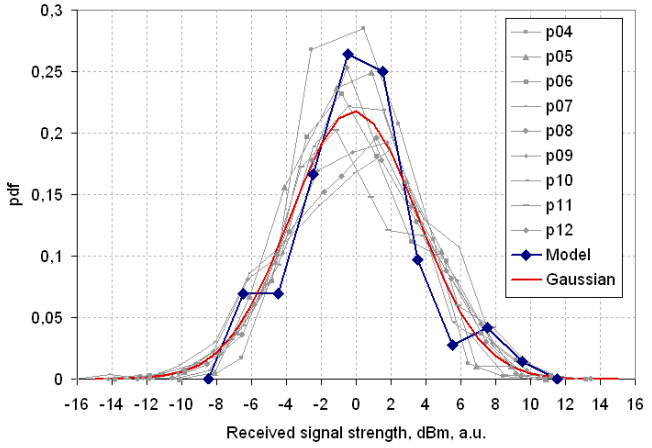


Fig. 23. Summarized and aligned RSS profiles of chaotically rotated hand held device in the LOS conditions. Solid blue line - modelled profile, solid red line - Gaussian-like profile $G(RSS)$.

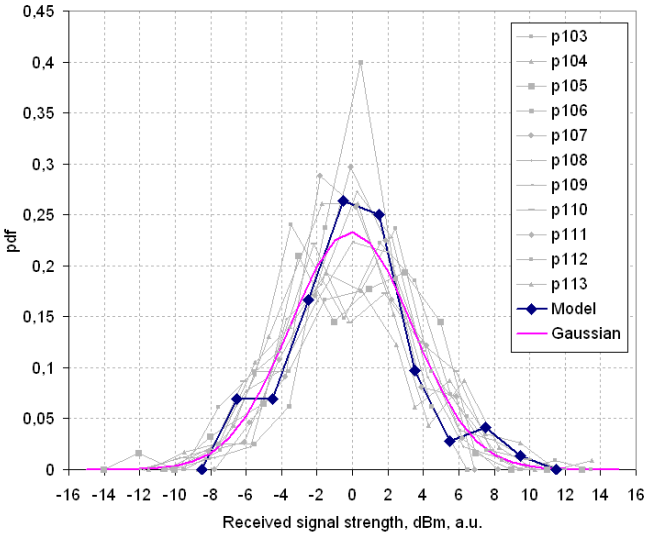


Fig. 24. Summarized and aligned RSS profiles of chaotically rotated hand held device in the NLOS conditions. Solid blue line - modelled profile, solid violet line - Gaussian-like profile $G(RSS)$.

all the profiles from Fig. 17, the centers of contours $RSS_{c,i}$ were determined, thus the differences $\Delta RSS_i = RSS_{c,i} - RSS_{c,model}$ were calculated. Then all contours were shifted by $\Delta RSS_i$ value along with horizontal axis. Fig. 23 contains all registered and modelled normalized symmetrical RSS profiles aligned to one central point for the data corresponding to LOS conditions indoors.

The blue polyline in Fig. 23 describes the modelled profile. The red curve corresponds to the Gaussian function

$$G_1(x) = \frac{a}{\sqrt{2\pi\sigma^2}} \exp(-\frac{(x-m)^2}{2\sigma^2}), \tag{7}$$

with the following parameters: $\sigma = 3.663$, $m = -0.122$, $a = 1.999$, the width on half-maximum is $\Delta_{FWHM,1} \approx 8.6$. $x$ is expressed in dB, $x = RSS_{c,i} - RSS_i$. Thus after substitution the RSS profile is

$$G_1(x) = 0.22 \cdot \exp(-\frac{x^2}{0.36 \cdot \Delta^2_{FWHM}}), or \tag{8}$$

$$G_1(x) = 0.22 \cdot \exp(-\frac{x^2}{26.8}). \tag{9}$$

The NLOS RSS profiles depicted in Fig. 17 were processed by the same method. The contours were aligned and fitted to Gaussian function. The result is presented in Fig. 24.

The violet curve is the Gaussian with the following parameters: $\sigma = 3.433$, $m = -0.071$, $a = 2.007$, the width on half-maximum is $\Delta_{FWHM,2} \approx 8.2$. The RSS profile is:

$$G_2(x) = 0.23 \cdot \exp(-\frac{x^2}{23.6}). \tag{10}$$

The RSS profile for rotating hand held device is LOS conditions indoors $G_1(x)$ is slightly broader than the profile in NLOS conditions $G_2(x)$. Probably additional reflections at close distances at the line-of-sight and Fresnel zones effects influence the broadening.

The functions (9) and (10) roughly describe variations in RSS for rotating hand held device in LOS and NLOS conditions correspondingly. The difference in contours is little,

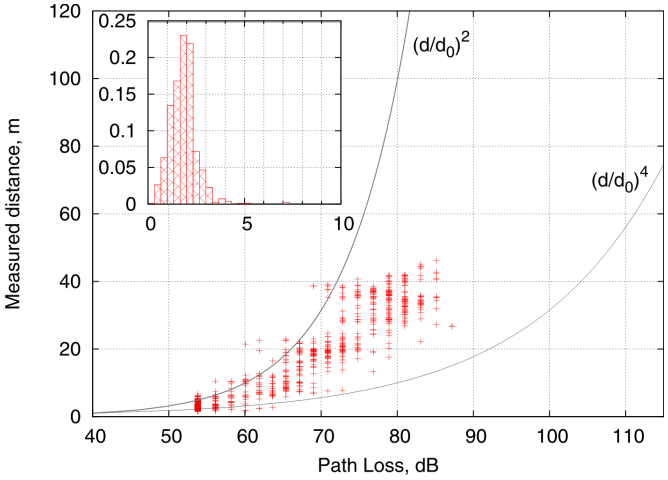


Fig. 25. Manually selected data from the Experiment 1, corresponding to the pure LOS conditions indoors

thus an assumption that the profile does not depend significantly on specific LOS/NLOS conditions was proposed. In the investigations described below the obtained profile $G_1(x)$ is used in the channel conditions identification algorithms as $f(PL)$ function (Section II-A).

## V. LOS ToF error profile

Though the measurement in the Experiment 3, Series 1 (Section III-D1) were carried out in LOS conditions, not all measurement data correspond to the criteria of low ToF errors. Thus in order to construct the model for the LOS ToF error profile, some data were manually selected. Those measurements with low ToF error value ($\varepsilon_i < [3.5..4]$ m) and with low $PL_i$ values are presented in Fig. 25.

The key parameters of the TEP presented in the inset histogram are: the steepness and the shape of the left wing, the

position of peak value, the width of peak on half-maximum and full width of the contour.

Since LOS TEP profile does not significantly depend on channel conditions, and taking into account LOS data from the other experiments outdoors (see Fig. 10), we propose to use the Rayleigh function as the model for LOS TEP. The probability density function of the Rayleigh distribution is

$$f(x;\sigma) = \frac{x}{\sigma^2} \cdot exp(-\frac{x^2}{2\sigma^2}). \quad (11)$$

Thus LOS TEP profile is described by the Rayleigh function with the peak value of 1 and the peak position of $\approx 1.2$ m:

$$TEP_{LOS}(\varepsilon) = 1.37 \cdot \varepsilon \cdot e^{-0.35 \cdot \varepsilon^2}, \varepsilon \in [0, \hat{d}]. \quad (12)$$

The graph of this function is presented in the Section VII.

## VI. NLOS ToF error profile

A set of graphs in Fig. 26 demonstrates the changes in TEPs corresponding to the constant measured distance $\hat{d}$ and different path loss values $PL_i$.

The ToF error profile summarized for all PL values and 33.0 m $\leq \hat{d} <$ 37.0 m is presented in Fig. 26a. Two peaks are easily identified: LOS case (the most probable ToF error lies in the range of 2-3 m on the horizontal axis of the inset histogram) and NLOS case (the center of the peak is 12 m).

Th intuitive idea discussed in the Introduction (Section I) corresponds to reality. For low path loss values (Fig. 26b) ranging error include only the LOS component. Then with increasing the path loss, the contribution of the LOS component to TEP decreases, whereas the contribution of NLOS component increases (Fig. 26c-d). For the path loss values $PL_i > 88$ dB no LOS component was observed (Fig. 26e-j).

The the NLOS ToF errors probability density function is described by a bell-like function. The center of the NLOS TEP corresponds to the ToF error of 12 m. The width of the NLOS TEP is approximately $\approx$ 14..15 m, and it does not significantly depend on the PL.

Thus, according to the data in Fig. 26, if ranging procedure returns, for example, $\hat{d} = 33.5$ m and $PL_i = 93$ dB, then the mean ToF error is equal to $\varepsilon_{mean} \approx 12$ m and the maximum variation is equal to $\approx \pm 7$ m.

The position of the mean ToF error and the width of the TEP depend on the measured distance value. In order to prove this statement and to derive the function, some data sets with the certain $\hat{d}_i$ and $PL_i$ values were extracted from the database and presented in Fig. 27.

All case presented in Fig. 27 correspond to NLOS scenario for the short (Fig. 27a) to long measured distances (Fig. 27e). For each TEP, the mean ToF error $\varepsilon_{mean}$ and the width of TEP $\Delta\varepsilon$ were obtained. For instance, for the measured distance $\hat{d} = 7$ m, $\varepsilon_{mean} \approx 3$ m and $\Delta\varepsilon \approx 6$ m, whereas for $\hat{d} = 37$ m, $\varepsilon_{mean} \approx 13$ m and $\Delta\varepsilon \approx 14$ m.

Obviously ToF error increases with the increasing the measured distance. The variation of ToF errors (width of TEP) increases as well. Mean ToF errors and widths of TEPs for all measured distances are presented in Fig. 28.

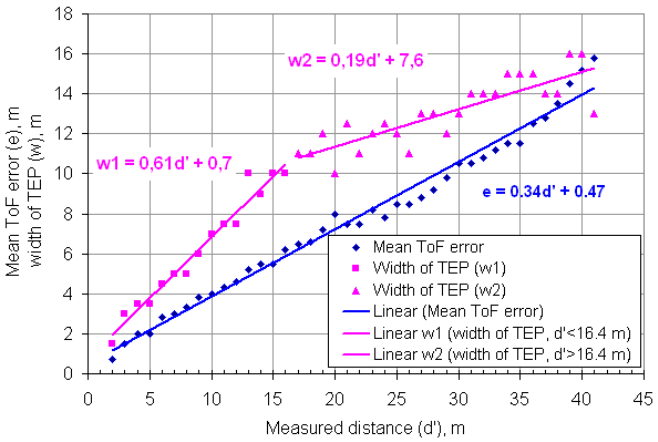


Fig. 28. Mean ToF error and width of ToF error profile dependencies on the measured distance

Mean ToF errors perfectly fit linear approximation. The corresponding functions is:

$$\varepsilon_{mean} = 0.34 \cdot \hat{d} + 0.47. \quad (13)$$

Thus, the position of the TEP roughly equals to $\frac{\hat{d}}{3}$.

Width of TEP is a more complex function of $\hat{d}$. It might be approximated by two linear functions with the intersection point at $\hat{d} \approx 16.42$.

$$\Delta\varepsilon = \begin{cases} 0.61 \cdot \hat{d} + 0.7, & \text{if } \hat{d} < 16.42 \\ 0.19 \cdot \hat{d} + 7.6, & \text{otherwise} \end{cases} \quad (14)$$

The NLOS ToF error profile might be modelled by a some bell-like function. Unlike the approach presented in [4] we propose to use more simple function – Gaussian. The center of the Gaussian corresponds to the mean ToF error $\varepsilon_{mean}$. The width is determined as follows. The parameter $\sigma$ in (6) is calculated so that the width of the Gaussian at 10% of the amplitude $A_0$ is equal to the experimentally obtained $\Delta\varepsilon$ value (14).

Thus NLOS TEP is expressed as:

$$TEP_{NLOS}(\varepsilon) = \exp(4 \cdot \ln 0.1 \cdot \frac{(\varepsilon - \varepsilon_{mean})^2}{(\Delta\varepsilon)^2}), \quad (15)$$

or

$$TEP_{NLOS}(\varepsilon) = \begin{cases} \exp(-9.21 \frac{(\varepsilon - 0.34 \cdot \hat{d} - 0.47)^2}{(0.61 \cdot \hat{d} + 0.7)^2}), \hat{d} < 16.42 \\ \exp(-9.21 \frac{(\varepsilon - 0.34 \cdot \hat{d} - 0.47)^2}{(0.19 \cdot \hat{d} + 7.6)^2}), \hat{d} \geq 16.42 \end{cases}. \quad (16)$$

The graphs of NLOS TEP ($\varepsilon \in [0, \hat{d}]$) built according to (16) for the measured distances $\hat{d} = 5, 10, 15, ..., 50$ m are presented in Fig. 29.

## VII. CombiTEP construction

One of the contributions of this paper is the proposed pdf for the LOS and NLOS errors of the measured distance estimations. If no prior data on the exact channel conditions (LOS or NLOS) is available, or if the conditions can not be definitely classified, then the pdf includes both the LOS and the NLOS components stated in (12) and (15) correspondingly.

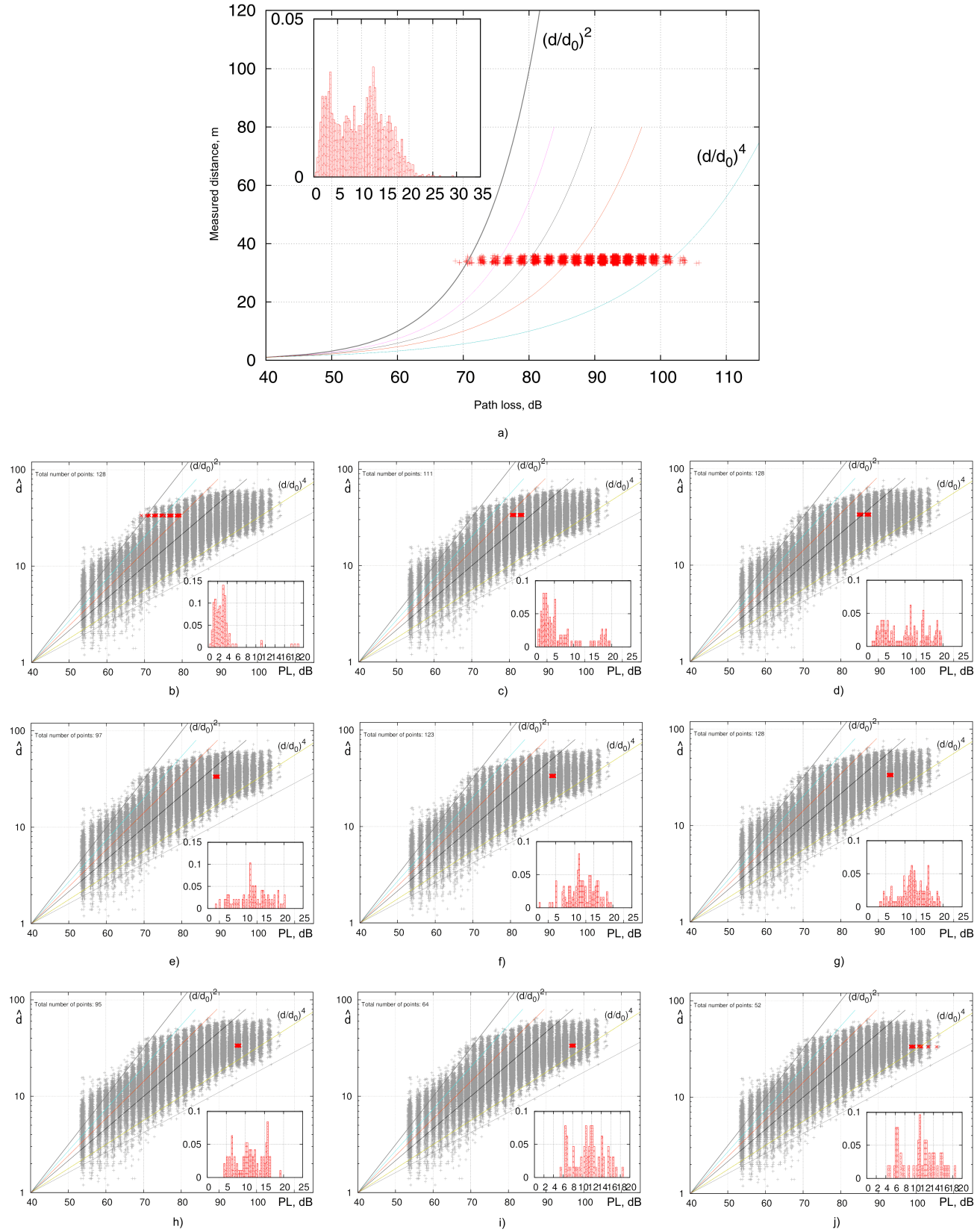


Fig. 26. Raw data (in main graphs) and the corresponding TEPs (in insets): a) summarized data for all $PL_i$ and 33.0 m$\leq \hat{d} <$ 37.0 m; b)-j) 33.0 $\leq \hat{d} <$ 34.0; b) $PL_i <$ 80 dB; c) $PL_i =$ 81..83 dB; d) $PL_i =$ 85..87 dB; e) $PL_i =$ 89 dB; f) $PL_i =$ 91 dB; g) $PL_i =$ 93 dB; h) $PL_i =$ 95 dB; i) $PL_i =$ 97 dB; j) $PL_i >$ 98 dB. Vertical axis is linear in case a), whereas it is logarithmic in cases b)-j). The histograms in insets are built only for data marked by red colour on the main graph.

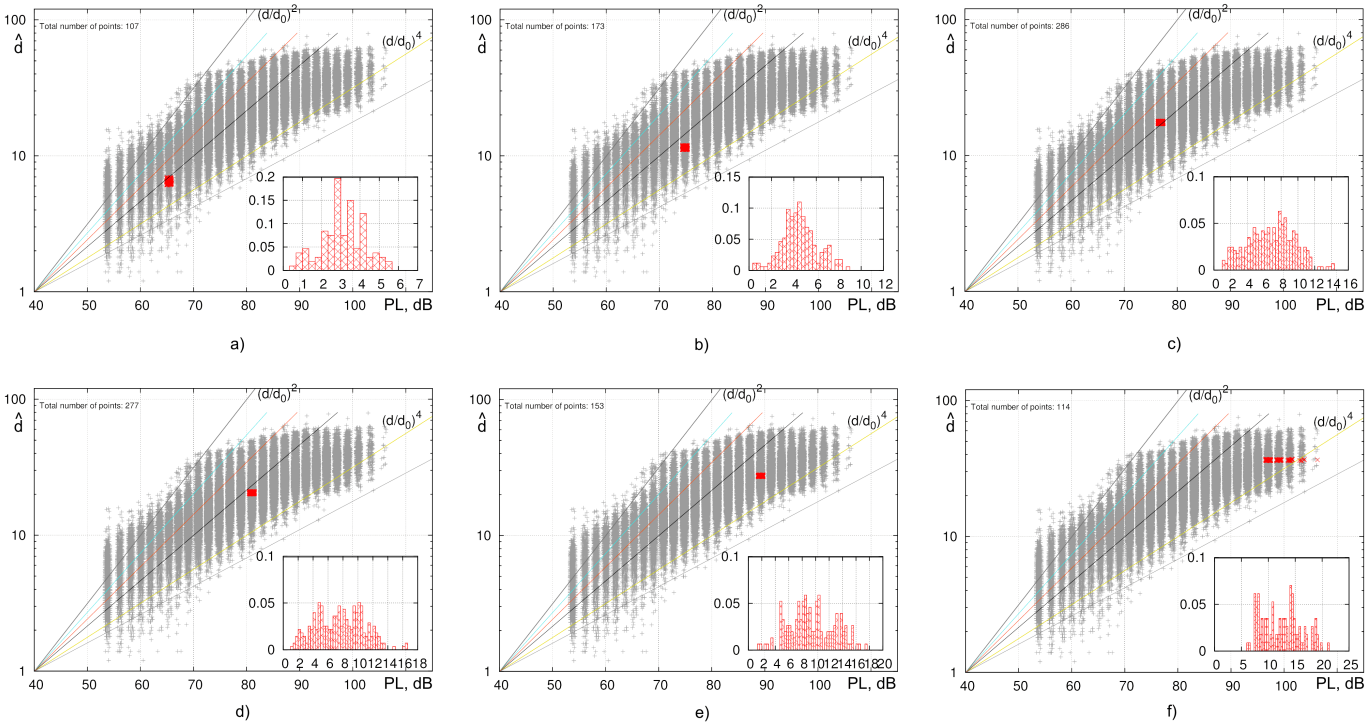


Fig. 27. Raw data (in main graphs) and the corresponding TEPs (in insets) in NLOS conditions: a) 6.0 m $\leq \hat{d} <$ 7.0 m and $PL_i = 65$ dB, mean ToF error $\varepsilon_{mean} \approx 3$ m, width of TEP is $\Delta\varepsilon \approx 6$ m; b) 11.0 m $\leq \hat{d} <$ 12.0 m and $PL_i = 75$ dB, $\varepsilon_{mean} \approx 4$ m, $\Delta\varepsilon \approx 8$ m; c) 17.0 m $\leq \hat{d} <$ 18.0 m and $PL_i = 77$ dB, $\varepsilon_{mean} \approx 6$ m, $\Delta\varepsilon \approx 12$ m; d) 20.0 m $\leq \hat{d} <$ 21.0 m and $PL_i = 81$ dB, $\varepsilon_{mean} \approx 7$ m, $\Delta\varepsilon \approx 12$ m; e) 27.0 m $\leq \hat{d} <$ 28.0 m and $PL_i = 89$ dB, $\varepsilon_{mean} \approx 10$ m, $\Delta\varepsilon \approx 14$ m; f) 36.0 m $\leq \hat{d} <$ 37.0 m and $PL_i > 96$ dB, $\varepsilon_{mean} \approx 13$ m, $\Delta\varepsilon \approx 14$ m. The histograms in insets are built only for data marked by red colour on the main graph.

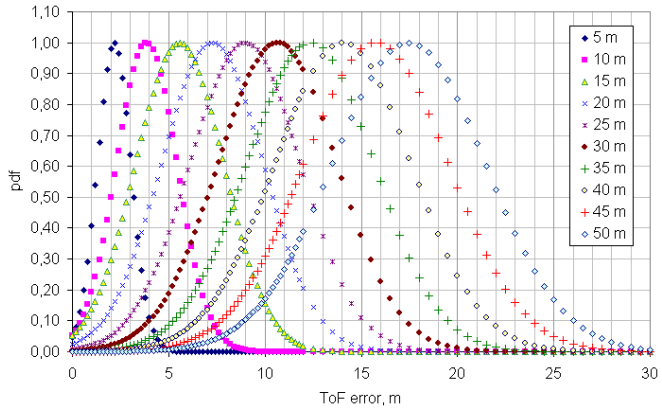


Fig. 29. NLOS ToF error profiles for the measured distances $\hat{d} = 5, 10, 15, 20, 25, 30, 35, 40, 45$ and 50 m. The width of each profile at 10% level of amplitude is equal to the experimentally obtained $\Delta\varepsilon$ value (14).

This combined profile (CombiTEP) describes the probability densities for the errors for the given $\hat{d}$ and $PL$.

In order to formulate the principles of the CombiTEP construction, a number of experimentally obtained ToF error profiles for some subsets of all obtained raw data presented in Fig. 4 should be discussed.

**Remark 1.** Fig. 30 presents TEPs for all data with 15.0 m $\leq \hat{d} <$ 16.0 m. Mean error is equal to 6 m (see the inset in Fig. 30a) and does not depend on the registered path loss (see Fig. 30c-l). It is characteristic that the NLOS component prevails the LOS component for all measured distances below 16 m. Only in case Fig. 30b, the LOS peak at 2-3 m is distinguishable. In other cases for $PL > 66$ dB (Fig. 30c-l), the TEP corresponds solely to the non-line-of-sight conditions.

**Remark 2.** To find the area on the plot in Fig. 4 describing NLOS data, the following technique was used. All data were separated in $N$ bins with certain measured distances $\hat{d}_n$, $n = 1..N$. The size of bins was set to 1 meter. Then the data in each bin were separated in $M$ bins with certain values of path loss $PL_m$, $m = 1..M$. Thus an array $Dat$ of $N * M$ was created. After that ToF error profile was obtained for the data in each cell $Dat_{nm}$ of this array.

Some TEPs are presented in Fig. 31. The first row of graphs (Fig. 31a-c) corresponds to $\hat{d} \approx 27.0$ m, the second (Fig. 31d-f) – to $\hat{d} \approx 31.0$ m, and the third (Fig. 31g-i) – to $\hat{d} \approx 41.0$ m. Three graphs in a row correspond to the adjacent path loss values. For example, the first row corresponds to $PL_i = 73$ dB, $PL_i = 75$ dB and $PL_i = 77$ dB.

Analysing the TEPs in one row from low to high path losses, a point of appearing the NLOS component can be registered. Subjectively cases a), d) and g) for $\hat{d}$ equal to 27 m, 31 m and 41 m contain practically no NLOS component. And for $PL > 74$ dB, $PL > 78$ dB, and $PL > 84$ dB the NLOS component can be identified.

After processing all the data the border limiting the NLOS area was obtained (see green circles in Fig. 32). This border seems to be fitted well with the exponent (linear function in

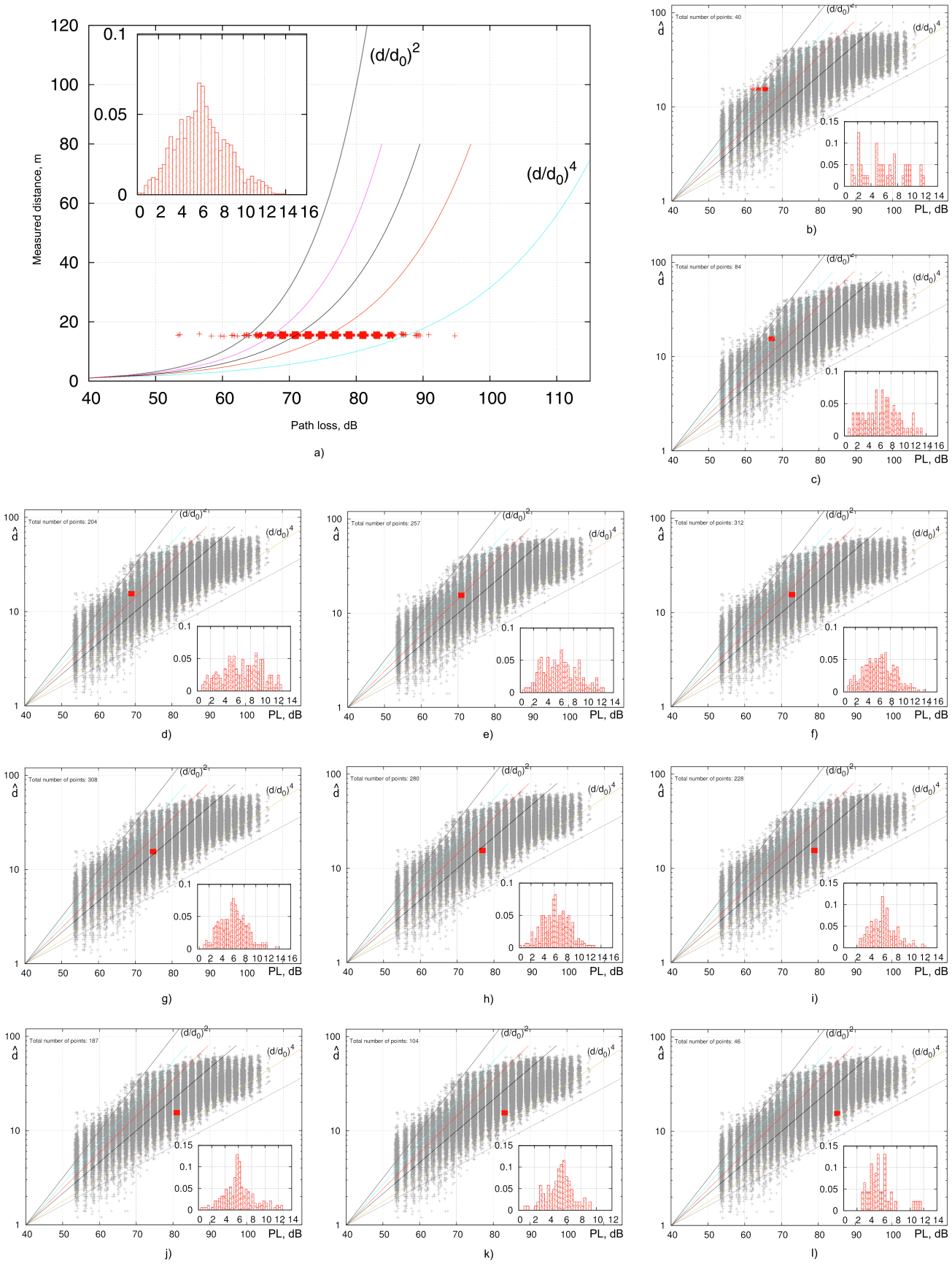


Fig. 30. Raw data for the measured distance 15.0 m $\leq \hat{d} <$ 16.0 m (in main graphs) and the corresponding TEPs (in insets): a) summarized data for all $PL_i$; b) $PL_i = 61..66$ dB; c) $PL_i = 67$ dB; d) $PL_i = 69$ dB; e) $PL_i = 71$ dB; f) $PL_i = 73$ dB; g) $PL_i = 75$ dB; h) $PL_i = 77$ dB; i) $PL_i = 79$ dB; j) $PL_i = 81$ dB; k) $PL_i = 83$ dB; l) $PL_i = 85$ dB. Vertical axis is linear in case a), whereas it is logarithmic in cases b)-l). The histograms in insets are built only for data marked by red colour on the main graph.

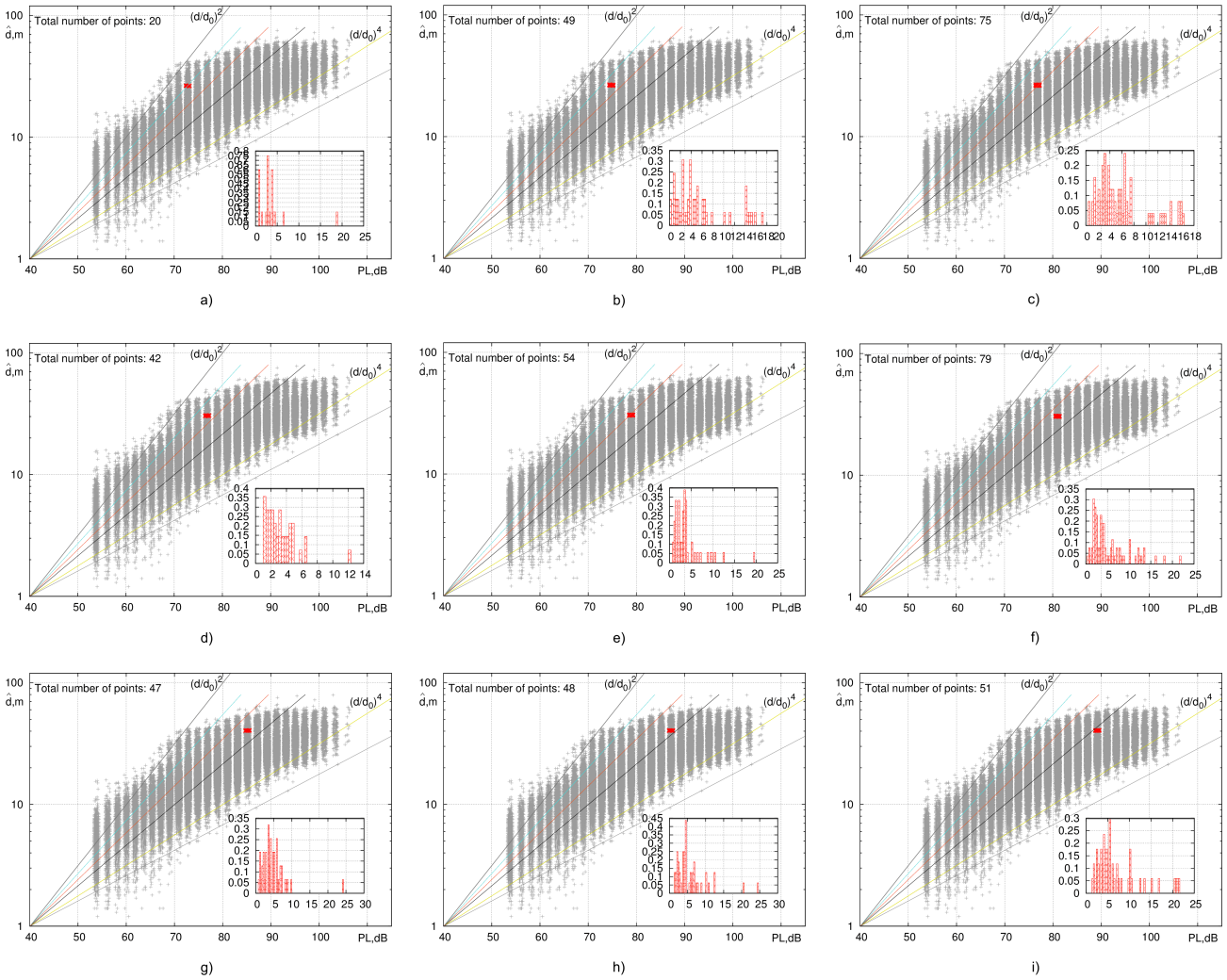


Fig. 31. NLOS border identification: a) 26.0 m $\leq \hat{d} <$ 27.0 m and $PL_i = 73$ dB; b) 26.0 m $\leq \hat{d} <$ 27.0 m and $PL_i = 75$ dB; c) 26.0 m $\leq \hat{d} <$ 27.0 m and $PL_i = 77$ dB; d) 30.0 m $\leq \hat{d} <$ 31.0 m and $PL_i = 77$ dB; e) 30.0 m $\leq \hat{d} <$ 31.0 m and $PL_i = 79$ dB; f) 30.0 m $\leq \hat{d} <$ 31.0 m and $PL_i = 81$ dB; g) 40.0 m $\leq \hat{d} <$ 41.0 m and $PL_i = 85$ dB; h) 40.0 m $\leq \hat{d} <$ 41.0 m and $PL_i = 87$ dB; i) 40.0 m $\leq \hat{d} <$ 41.0 m and $PL_i = 89$ dB. TEPs in cases a), d) and g) for $\hat{d}$ equal to 27 m, 31 m and 41 m contain practically no NLOS component. TEPs in cases b), e) and h) reveal a tiny contribution of NLOS. Cases c), f) and j) correspond to the stronger NLOS signal, than in the cases b), e) and h).

lognormal scale graph):

$$\hat{d} = 2.777 \cdot 10^{\frac{PL}{74.74}}. \tag{17}$$

All data points below the border line have strong NLOS component. All data points above this limit have little or no NLOS contribution.

**Remark 3.** LOS TEP must be included in CombiTEP in any case, since there is a not null probability to register very weak signal, however in LOS conditions, for example, attenuated by walls.

The equation corresponding to the path loss exponent $\beta = 1.7$ is:

$$PL_{LOS} = 17 \cdot \lg \frac{\hat{d}}{0.00444}. \tag{18}$$

**Remark 4.** The NLOS border is not sharp. Thus some dispersion should be introduced in the CombiTEP model in order to blur the transitional area from pure NLOS (to the right) to LOS region (to the left). We propose to use the obtained profile $G_1(x)$ (9) for this purpose.

As it was said the NLOS border corresponds to the conditions of appearing NLOS effect. Thus the line of strong NLOS is lying somewhere to the right. It is believed that this line of strong NLOS is parallel to the NLOS border presented in Fig. 32 and shifted by $\xi_1$ dB ($\xi_1 > 0$) to the right. Therefore the equation is the following.

$$D_{NLOS}(PL) = 2.777 \cdot 10^{\frac{PL_c}{74.76}}, \tag{19}$$

where $PL_c = PL - \xi_1$.

According to the Remark 2 and (19), if $\hat{d} < D_{NLOS}(\hat{PL})$ (or $\hat{PL} > PL_c$), then it is assumed that the measurement ($\hat{d}$, $\hat{PL}$) was done in conditions of NLOS, and CombiTEP should include maximum NLOS TEP. Otherwise the weight of NLOS TEP in CombiTEP should be calculated as a function of difference between $\hat{PL}\,|_{\hat{d}}$ and the point $PL_c\,|_{\hat{d}}$ on the left

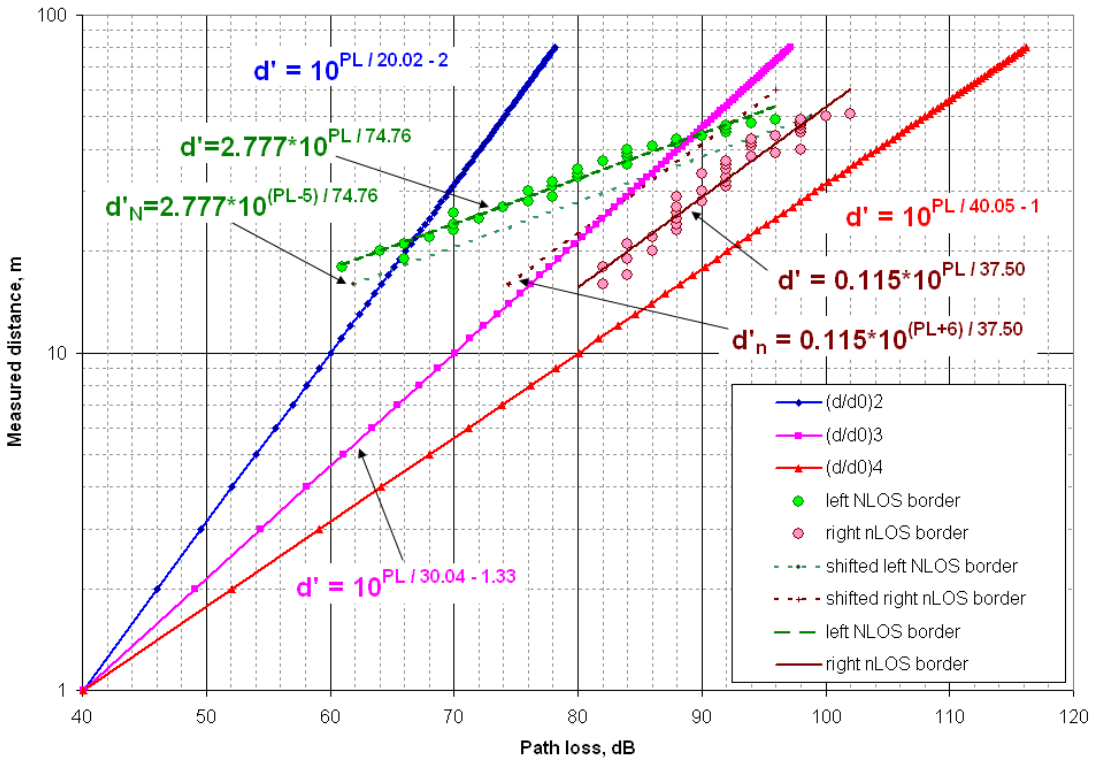


Fig. 32. NLOS area identification. Blue line with diamonds – path loss exponent $\beta = 2$; violet line with squares – path loss exponent $\beta = 3$; red line with triangles – path loss exponent $\beta = 4$; green circles – manually selected points of the left NLOS border; green line – the left NLOS border (no NLOS measurements were observed to the left of the NLOS border, all data points below or to the right of the green line have strong NLOS component); green dashed line – the left NLOS border shifted to the right by 5 dB; brown circles – manually selected points of the right nLOS border; brown line – the right nLOS border (almost no LOS and nLOS measurements were observed to the right of the nLOS border, data points above or to the left of the brown line might correspond to the nLOS scenario); brown dashed line – the right nLOS border shifted to the left by 6 dB.

NLOS border using (9):

$$G(\hat{PL}) = \exp(-\frac{(\hat{PL} - PL_c)^2}{26.8}), \quad (20)$$

where the amplitude of the Gaussian is set to 1. If the shift to the right is $\xi_1 = 5$, the equation for the left NLOS border $PL_{NLOS}$ is the following.

$$PL_{NLOS} = 74.76 \cdot \lg \frac{\hat{d}}{2.38} \quad (21)$$

This formula is presented in Fig. 32 as green dashed line (the left NLOS border shifted to the right by 5 dB).

**Remark 5.** As it could be seen from Fig. 31d-g the widths of left peaks in insets do not correspond to the LOS TEP discussed in Section V. These peaks are significantly wider than the LOS TEP for all measured distances above ≈20 m. The most probable ToF error values are in the range from 2 to 5 m. Hereinafter we will refer to this peak as to near-LOS (nLOS) case.

Analysing the TEP data presented in insets in Fig. 26, the nLOS component is strong in Fig. 26b-c, moderate in Fig. 26d, weak in Fig. 26e and absent in Fig. 26f-j. Thus the path loss value corresponding to the right nLOS border is $PL = 90$ dB for $\hat{d} \approx 34$ m.

Such points for all measured distances are presented as brown circles in Fig. 32. The approximated line through these points

$$D_{nLOS}(PL) = 0.115 \cdot 10^{\frac{PL}{37.50}} \quad (22)$$

is similar to the line with the path loss exponent $\beta \approx 3.5$ (2). Almost no LOS and nLOS measurements were observed to the right of this nLOS border.

Alike the left NLOS border, the right nLOS border is not sharp. In order to model the data around this line and to diffuse the border, using the same technique as in the Remark 4, the equation for the right nLOS border $PL_{nLOS}$ shifted to the left by $\xi_2 = 6$ dB is the following.

$$PL_{nLOS} = 37.5 \cdot \lg \frac{\hat{d}}{0.166} \quad (23)$$

This curve is presented in Fig. 32 as brown dashed line (the right nLOS border shifted to the left by 6 dB).

**Remark 6.** To model the nLOS TEP, Rayleigh distribution (11) was used.

$$TEP_{nLOS}(\varepsilon) = 0.49 \cdot \varepsilon \cdot e^{-0.043 \cdot \varepsilon^2}, \varepsilon \in [0, \hat{d}] \quad (24)$$

The peak of TEP is located at $\varepsilon \approx 3.4$ m. The most probable values of ToF error $\varepsilon$ are in the range from 2 m to 5 m.

### A. CombiTEP model

As it was proposed above, the LOS TEP is described by the Rayleigh distribution with the constant width and the peak at 1.2 m (12), the nLOS TEP – by the Rayleigh distribution with the constant width and peak at 3.4 m (24), and the NLOS TEP – by the Gaussian with width and peak position depending on the measured distance (16).

The TEPs for LOS, nLOS and NLOS with the amplitudes equal to 1 are drawn in Fig. 33. The presented NLOS TEP corresponds roughly to the measured distance $\hat{d} \approx 36$ m, thus the the peak value is at $\varepsilon \approx 12$ m and the width is $\Delta\varepsilon \approx 14$ m according to the (13, 14) and Fig. 28.

The combined TEP is modelled as the weighted sum of three components.

$$W_{\kappa\mu\nu}(\varepsilon) = \kappa \cdot TEP_{LOS}(\varepsilon) + \mu \cdot TEP_{nLOS}(\varepsilon) + \nu \cdot TEP_{NLOS}(\varepsilon) \quad (25)$$

The coefficients $\kappa$, $\mu$, and $\nu$ set the weights of LOS, nLOS and NLOS summands correspondingly. After these coefficients are defined, the normalization procedure might be applied to $W_{\kappa\mu\nu}(\varepsilon)$ function in order to use the CombiTEP in localization algorithms.

The contribution of LOS, nLOS and/or NLOS profiles in the combined TEP differs from case to case. An example of summation in equal proportions $(1:1:1)$ is presented in Fig. 33 as green line. For the ratio of $LOS : nLOS : NLOS = 3:1:5$ (NLOS component is stronger than LOS, and LOS is stronger than nLOS), the corresponding CombiTEP is described by the curve from red triangles. In both examples the probability density function of the ToF error for $\hat{d} = 36$ m consists of 2 peaks: one matches LOS scenario, another – NLOS.

### *B. Determination of weights in the CombiTEP model*

The coefficients $\kappa$, $\mu$, and $\nu$ are defined by a simple algorithm based on the assignment of a single set of the measured data $(\hat{d}, \hat{PL})$ to a particular category.

If $\hat{d} < 16.42$ m, then it is assumed that the CombitTEP consists only of the NLOS component with a small contribution of the LOS component. Therefore, $\kappa = 0.1$, $\mu = 0$ and $\nu = 1$. Otherwise, the following steps must be performed. The illustration to the proposed algorithm is presented in Fig. 34.

**1.** For the obtained set of the measured data $(\hat{d}, \hat{PL})$, the values of path loss on three borders are calculated $PL_{c1} = PL_{LOS}(\hat{d})$, $PL_{c2} = PL_{nLOS}(\hat{d})$, $PL_{c3} = PL_{NLOS}(\hat{d})$ according to (18), (23) and (21) respectively.

**2.** The function describing the coefficient $\nu$ is the Gaussian to the left of $PL_{c3}$ and is flat to the right of $PL_{c3}$ (see Fig. 34c).

Thus, if $\hat{PL} < PL_{c3}$, then $\nu = G(\hat{PL})$ (20), else $\nu = 1$.

**3.** To the right of $PL_{c2}$ (see Fig. 34b), the coefficient $\mu$ corresponds to the nLOS component and is described by the Gaussian. The weight of the nLOS component decreases rapidly with the increase of the path loss. To the left of the nLOS border the situation is not so clear. Obviously the contribution of the nLOS in the CombiTEP should be weaker for lower path losses. Thus the linear function was proposed to model $\mu(PL)$. $\mu(PL_{c2}) = 1$, $\mu(PL_{c1}) = 0$.

Thereby, if $\hat{PL} > PL_{c2}$, then $\mu = G(\hat{PL})$ (20), else if $\hat{PL} < PL_{c1}$, then $\mu = 0$, else $\mu = \frac{\hat{PL} - PL_{c1}}{PL_{c2} - PL_{c1}}$.

**4.** The LOS component is strong at low path loss values and becomes weaker with increasing the path loss. The linear function was chosen to model the weight of the LOS component (see Fig. 34a). However for the larger PL values, $\kappa$ is not equal to zero. Obstacles on the way of electromagnetic waves might suppress both the LOS and the NLOS components in multipath propagation. And even for low measured distances, very high path loss values could be registered.

Accordingly, if $\hat{PL} < PL_{c1}$, then $\kappa = 1$, else $\kappa = \frac{PL_{c2} - \hat{PL}}{PL_{c2} - PL_{c1}}$. If $\kappa < 0.1$, then $\kappa = 0.1$.

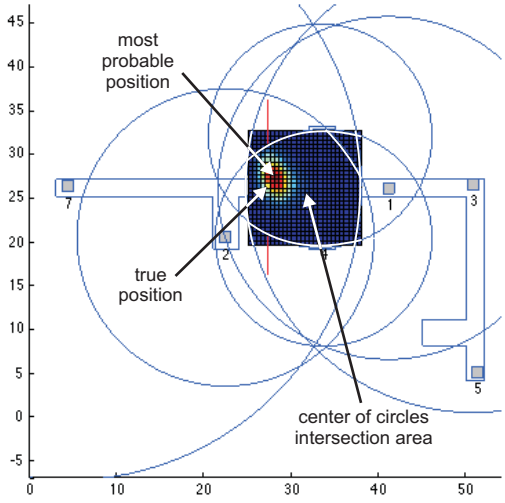


Fig. 35. Utilization of the CombiTEP model. Units in the vertical and horizontal axes – meters. The radii of circles are equal to the measured distances.

## VIII. CombiTEP utilization

The proposed model for the CombiTEP can be used in many localization algorithms. In the case, presented in Fig. 35 6 distances and path losses were measured between a mobile node and anchors. The true position of the mobile node was in the center of long corridor.

One of the simple methods of location calculation determines the position of the object as the center of the circles intersection area. The error is approximately 5 m.

In order to estimate the feasibility of the developed technique, we built 6 CombiTEPs corresponding to 6 measurements. The final probability density function was defined as the product of 6 CombiTEPs. All the area of circles intersections was divided into tiles. The size of a tile was 0.5 m. For each tile the value of the final pdf was calculated. Brown and red colours in Fig. 35 correspond to high values. Blue colour – to low values.

The distance between the true and the most probable positions was 1.5 m. So the positioning accuracy significantly increased.

## IX. Conclusion

ONLY IDEAS BELOW.

The raw data were fitted with analytical function.

In the presented model the conditions of near LOS (nLOS) are discussed. Probably nLOS corresponds to the conditions between LOS and soft NLOS, possibly partly including soft NLOS.

It is impossible to determine the channel conditions (LOS or NLOS) for the measured distances lower than 15 meters

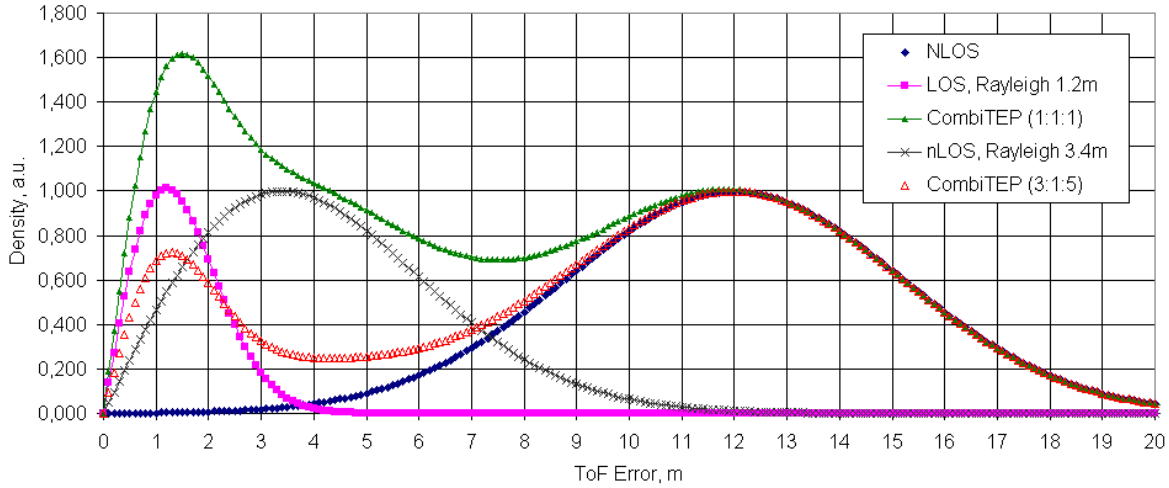


Fig. 33. The example of CombiTEP construction from LOS, nLOS and NLOS ToF error profiles. Violet squares – LOS TEP with the peak value at $\varepsilon \approx 1.2$ m; gray crosses – nLOS TEP with the peak value at $\varepsilon \approx 3.4$ m; blue diamonds – the example of NLOS TEP with the peak value at $\varepsilon \approx 12$ m and the width $\Delta\varepsilon \approx 14$ m; green triangles – the example of CombiTEP with the ratio $LOS : nLOS : NLOS = 1 : 1 : 1$; red triangles – the example of CombiTEP with the ratio $LOS : nLOS : NLOS = 3 : 1 : 5$.

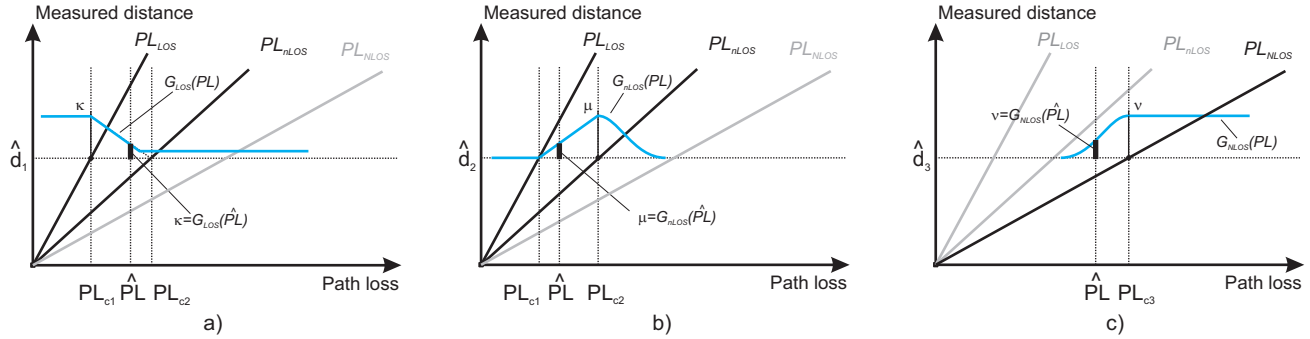


Fig. 34. Determination of weights $\kappa$ (a), $\mu$ (b) and $\nu$ (c) in the CombiTEP model. Blue lines correspond to the dependencies of weights $\kappa$, $\mu$ and $\nu$ on the path loss. $PL_{c1}$, $PL_{c2}$ and $PL_{c3}$ are the points of intersection of lines $\hat{d} = \hat{d}_1$, $\hat{d} = \hat{d}_2$ and $\hat{d} = \hat{d}_2$ with three borders for LOS, nLOS and NLOS cases respectively.

basing only on ToA and RSS measurements since variations of mutual orientations of two modules are greater than variance in RSS corresponded to other factors.

All the obtained results correspond to common environment (they consider human body effect and various orientation of devices).

!! NLOS detection, NLOS mitigation

!! The statistics for LOS and NLOS bias errors were obtained.

It is clear that region $>$ 40 m contains strong nLOS component.

Authors observed TEP narrowing for large PL values at some distances.

Other context information might be used to define $\kappa$, $\mu$, and $\nu$.

## ACKNOWLEDGMENT

The authors would like to thank Maria Serezhina, Maria Davydova and Elena Mehnetsova for the help in organization of the measurement campaign.

## REFERENCES

[1] S. Venkatesh and R. M. Buehrer, "Nlos mitigation using linear programming in ultrawideband location-aware networks," *IEEE Transactions on Vehicular Technology*, vol. 56, no. 5, pp. 3182–3198, 2007.

[2] F. Montorsi, F. Pancaldi, and G. M. Vitetta, "Statistical characterization and mitigation of nlos errors in uwb localization systems," in *IEEE International Conference on Ultra-Wideband, ICUWB*, 2011, pp. 86–90.

[3] S. Al-Jazzar and J. Caffery, "New algorithms for nlos identification," in *Proc. of the 14th IST Mobile Wireless Commun. Summit*, vol. June, 2005, pp. 1–5.

[4] S. Venkatesh and R. M. Buehrer, "Nlos identification in ultrawideband systems based on received signal statistics," *IET Microw. Antennas Propag.: Special Issue on Antenna Systems and Propagation for Future Wireless Communications*, vol. 1, no. 6, pp. 1120–1130, 2007.

[5] S. Marano, W. Gifford, H. Wymeersch, and M. Win, "Nlos identification and mitigation for localization based on uwb experimental data," *IEEE Journal on Selected Areas in Communications*, vol. 28, no. 7, pp. 1026–1035, 2010.

[6] S. Venkatraman and J. Caffery, "A statistical approach to non-line-of-sight bs identification," in *The 5th International Symposium on Wireless Personal Multimedia Communications*, vol. 1, 2002, pp. 296–300.

[7] J. Khodjaev, Y. Park, and A. S. Malik, "Survey of nlos identification and error mitigation problems in uwb-based positioning algorithms for dense environments," *Ann. Telecommun., 65:301-311*, 2010.

[8] P.-C. Chen, "A non-line-of-sight error mitigation algorithm in location estimation," in *IEEE Wireless Communications and Networking Conference, WCNC*, vol. 1, 2005, pp. 316–320.

[9] A. F. Molisch, K. Balakrishnan, C.-C. Chong, S. Emami, A. Fort, J. Karedal, J. Kunisch, H. Schantz, U. Schuster, and K. Siwiak, "Ieee 802.15. 4a channel model-final report," *Tech. Rep., Document IEEE 802.1504-0062-02-004a*, 2005.
[10] S. Ghassemzadeh, R. Jana, C. Rice, W. Turin, and V. Tarokh, "Measurement and modeling of an ultra-wide bandwidth indoor channel," *IEEE Transactions on Communications*, vol. 52, no. 10, pp. 1786–1796, 2004.
[11] G. Pedersen, K. Olesen, and S. Larsen, "Bodyloss for handheld phones," in *IEEE 49th Conference on Vehicular Technology*, vol. 2, 1999, pp. 1580–1584.
[12] J. Krogerus, J. Toivanen, C. Icheln, and P. Vainikainen, "Effect of the human body on total radiated power and the 3-d radiation pattern of mobile handsets," *IEEE Transactions on Instrumentation and Measurement*, vol. 56, no. 6, pp. 2375–2385, 2007.
[13] A. Moschevikin, A. Galov, A. Soloviev, A. Mikov, A. Volkov, and S. Reginya, "Realtrac technology overview," *EvAAL 2013, Communications in Computer and Information Science series CCIS*, vol. 386, pp. 60–71, 2013.
[14] N. Alsindi, C. Duan, J. Zhang, and T. Tsuboi, "Nlos channel identification and mitigation in ultra wideband toa-based wireless sensor networks," in *6th Workshop on Positioning, Navigation and Communication, WPNC-2009*. IEEE, 2009, pp. 59–66.
[15] A. Chehri and P. Fortier, "Measurements and modeling of line-of-sight uwb channel in underground mines," in *IEEE Global Telecommunications Conference, GLOBECOM '06*, 2006, pp. 1–5.
[16] O. W. Ata, M. S. Ala'Eddin, M. I. Jawadeh, and A. I. Amro, "An indoor propagation model based on a novel multi wall attenuation loss formula at frequencies 900 mhz and 2.4 ghz," *Wireless Personal Communications*, vol. 69, no. 1, pp. 23–36, 2013.
[17] A. Moschevikin, A. Galov, S. Reginya, A. Volkov, and A. Sikora, "The impact of nlos components in time-of-flight networks for indoor positioning systems," in *The 7th IEEE International Conference on Intelligent Data Acquisition and Advanced Computing Systems, IDAACS-2013*, 2013.

PLACE PHOTO HERE

**Alex Moschevikin** graduated from the Petrozavodsk State University (PetrSU) in 1993, received PhD degree in physical electronics from PetrSU, Russian Federation, in 1999.

Since 1999 he is with PetrSU as an associate professor at Faculty of Physical Engineering. From 2002 to 2008 he was the coordinator and the head of the Technology Transfer Office of the Research and Educational Center "Plasma" of PetrSU. He is a member of the Council of PetrSU on computer sciences and innovations.

He is currently a chief science officer of small innovative enterprises RTL-Service Ltd. and Nanonets Ltd., Russian Federation. In April 2011 RTL-Service Ltd. was awarded by the acknowledgement letter for the achievements in innovation activity by the Head of Republic of Karelia.

Dr. Moschevikin is the head of the research team (25 developers) which carried out several projects on real time location systems, wireless sensors networks, automation, computer nets, Internet technologies and distributed remote software and hardware development. He was a Principal Investigator or supervisor in more than 20 research projects of regional, national and international organizations. The products of RTL-Service ltd. won several prizes at International exhibitions.

In 2010 he was awarded by the honorary certificate of the Ministry for Education and Science of Russian Federation for achievements in research and educational activity, great contribution in training of high qualification specialists.

**Sergey Reginya** received the B.Tech and M.Tech degrees at Faculty of Physical Engineering of Petrozavodsk State University, Russian Federation, in 2010 and 2012, respectively.

Currently he is a PhD student at the Petrozavodsk State University, and an engineer at innovative company Nanonets Ltd, Russian Federation. His research interests include wireless sensors networks, indoor radio signals propagation, pressure sensors utilization, and local positioning systems algorithms.

**Jane Doe** Biography text here.